Finite-element modelling based on optical coherence tomography and corresponding X-ray microCT data for three human middle ears

Marzieh Golabbakhsh[1], Xuan Wang [1], Dan MacDougall [3], Joshua Farrell [3], Thomas Landry [3], W. Robert J. Funnell[1,2], Robert Adamson [3,4]
J. Assoc. Res. Otolaryngol. 24(3): 339-363 (2023)

[1] Department of BioMedical Engineering, McGill University, Montréal, QC, Canada
[2] Department of Otolaryngology – Head & Neck Surgery, McGill University, Montréal, QC, Canada
[3] School of Biomedical Engineering, Dalhousie University, Halifax, NS, Canada
[4] Electrical and Computer Engineering Department, Dalhousie University, Halifax, NS, Canada

Email addresses:
marzgol@gmail.com
xuan.wang.univ@gmail.com
dan.ryan.macdougall@gmail.com
josh.farrell@dal.ca
tglandry@dal.ca
robert.funnell@mcgill.ca
rob.adamson@dal.ca

This version of the article has been accepted for publication, after peer review, but is not the Version of Record and does not reflect post-acceptance improvements, or any corrections. The Version of Record is available online at http://dx.doi.org/10.1007/s10162-023-00899-x. Use of this Accepted Version is subject to the publisher's Accepted Manuscript terms of use (https://www.springernature.com/gp/open-research/policies/accepted-manuscript-terms).

ACKNOWLEDGEMENTS

This work was supported in part by the Canadian Institutes of Health Research and the Natural Sciences and Engineering Research Council of Canada.

STATEMENTS

Adamson, MacDougall and Farrell declare financial interest in a startup company, Audioptics Medical, working to commercialize middle-ear OCT technology. The other authors declare that they have no conflicts of interest.

ABSTRACT

Purpose

Optical coherence tomography (OCT) is an emerging imaging modality which is non-invasive, can be employed in vivo, and can record both anatomy and vibrations. The purpose here is to explore the application of finite-element (FE) modelling to OCT data.

Methods

We recorded vibrations for three human cadaver middle ears using OCT. We also have X-ray microCT images from the same ears. Three FE models were built based on geometries obtained from the microCT images. The material properties and boundary conditions of the models were obtained from previously reported studies.

Results

Tympanic-membrane (TM) vibration patterns were computed for the three models and compared with the patterns measured using OCT. Frequency responses were also computed for all three models for several locations in the middle ear and compared with the OCT displacements and with the literature. The three models were compared with each other in terms of geometry and function. Parameter sensitivity analyses were done and the results were compared among the models and with the literature. The simulated TM displacement patterns are qualitatively similar to the OCT results. The simulated displacements are closer to the OCT results for 500 Hz and 1 kHz but the differences are greater at 2 kHz.

Conclusion

This study provides an initial look at the combined use of OCT measurements and FE modelling based on subject-specific anatomy. The geometries and parameters of the existing FE models could be modified for individual patients in the future to help identify abnormalities in the middle ear.

KEYWORDS

Finite-element modelling, optical coherence tomography, middle ear, human, microCT, vibration measurement

1. INTRODUCTION

Quantitative models of the middle ear using the finite-element (FE) method can help to understand the underlying causes of hearing loss. FE middle-ear models were first created for animal ears [1]. Since then, several groups have developed human FE middle-ear models, [e.g., 2–10]. A middle-ear model definition includes material-property parameters, geometry and boundary conditions. Over the years there have been many studies of the effects of varying material properties on middle-ear sound transmission in FE models, but few modelling studies have considered how anatomical variations [e.g., 11–15] affect function. Some FE modelling studies have looked at the effects of tympanic-membrane (TM) shape [1, 16, 17]. Motallebzadeh et al. [10] and De Greef et al. [18] also investigated the effects of anatomical variability in FE models.

Optical coherence tomography (OCT) is based on low-coherence interferometry, typically with near-infrared light. A recent technical review by Ramier et al. [19] describes the history of OCT for imaging the middle ear and inner ear. Pitris et al. [20], Heerman et al. [21], Djalilian et al. [22] and Just et al. [23] were early users of OCT for middle-ear imaging, and more recently OCT has been used to measure TM thickness in normal and pathological ears [24, 25, 25]. OCT Doppler vibrometry can be used to record motions of the middle ear along with structural imaging [26–29]. MacDougall et al. [29] were the first to do OCT measurements of middle-ear vibrations in live subjects.

There have been few studies of the full-field vibration patterns of the TM in human ears, as distinct from measurements at one or a few points. Tonndorf and Khanna [30] used time-averaged holography in human cadaver ears for the first time, and much later stroboscopic holography was used [31, 32]. Recently, Tang et al. [33] used a high-speed digital holography system to measure both the shape and the displacements of the TM. These studies all described simple patterns of the TM surface displacement occurring at frequencies below 2 kHz, where the different parts of the TM move in-phase with one to three maxima on the TM. They reported that at frequencies above 2 kHz, the pattern of the displacement becomes more complicated; the number of local maxima increases, and the different maxima are not in phase. OCT measurements are a new way to study TM vibration patterns [29]. In addition to simultaneously imaging the anatomy of the middle ear, OCT vibrometry gives us the opportunity to noninvasively observe the displacement patterns of the whole middle ear, including both the TM and the ossicles.

The validation of computational models has usually been done based on data from different ears than the ones on which the models' geometry were based. Mikhael et al. [6], on the other hand, used experimental data measured by means of laser Doppler vibrometry for the validation of a model whose geometry was built from high-resolution microCT data for the same specimen. Model validation with OCT is potentially powerful because we can evaluate the behaviour of multiple parts of the same middle ear using both geometry and vibration from the OCT data.

FE modelling of a cadaver ear using microCT data in combination with both anatomy and vibration OCT data was introduced by our McGill University and Dalhousie University groups [34]. In this paper we present that model and two new models, and the simulated vibrations of the models are compared to the corresponding OCT vibration measurements. We present a parameter sensitivity analysis and compare the behaviours of the three models.

2. METHODS

Data

Specimens were the right cadaver ear of a 76-year-old Caucasian male and the right and left ears of a 66-year-old Caucasian male. We have both microCT and OCT data for these cadaver ears. Data were recorded in 2016 Feb (ear 2016-1) and 2017 Jun (ears 2017-1 and 2017-2) at Dalhousie University. The OCT data include B-mode (brightness) structural images and D-mode (Doppler) vibration images. B-mode images are generated at a nominal frame-rate of 20 frames per second (FPS) and the system was configured for 128×128×330-voxel 3D B-mode imaging at about 0.15 volumes per second. A full 3D D-mode volume containing 128 slices of 128×330 images was collected and processed over a total acquisition time of 70 minutes. Our OCT system consists of a Vernier-tuned distributed Bragg-reflector akinetic swept laser (Insight Photonics Solutions, Model SLE-101, central wavelength λ =1550 nm, tuning bandwidth = 40 nm, nominal repetition rate f_s = 100 kHz, nominal power P_0 = 20 mW). This system has a fast sweeping rate and a long coherence length, l_c > 200 mm, which gives the possibility of imaging the full depth of the human middle ear. The ear canal was partially drilled away to aid alignment of the system for imaging. The field of view of the laser was designed to be 10×10 mm. During the OCT recording, a sound stimulus of 100 dB SPL (2 Pa_{rms}) was applied to the TM through a tube speaker (Etymotic Research, ER3A) and a speculum (Figure 1). The stimulus was delivered through a tube located within 3 mm of the TM and near to the annulus to keep the sound tube out of the OCT field of view. The wavelengths at the frequencies involved here are so long that the sound-pressure field will be practically uniform across the TM and between the tip of the sound-delivery tube and the TM. The sound pressure level was monitored using a calibrated tube microphone (Etymotic Research, ER7C Series B). This system was previously described by MacDougall et al. [29].

The OCT data for each ear include peak-to-peak displacements for three frequencies: 500 Hz, 1 kHz and 2 kHz for ears 2017-1 and 2017-2, and only 500 Hz for ear 2016-1. For each frequency there are two volumes of static B-mode images (before and after Doppler OCT recording) and a volume of D-mode images. The microCT images were acquired using a Triumph II PET/SPECT/CT scanner (TriFoil Imaging, Chatsworth, California). The X-ray energy was set to 75 kVp. The microCT images for each ear contain 512 sections of 512×512 pixels each. The isotropic voxel size is 81 μm.

Software

OCT animation software (Animator) was developed by the Dalhousie group and uses a GPU and CUDA (Nvidia). The software uses a ray-casting approach to volume rendering of the OCT data [35] to create 3D volumetric images (Figure 2). The software can also produce 3D visualizations that fuse B-mode and D-mode data to show the harmonic response of the tissues in response to sound as an animated, exaggerated displacement, moving during a harmonic excitation. This can be used to qualitatively analyze the displacement results from the OCT measurements.

The Fie program (developed in our lab along with Tr3 and Fad (http://audilab.bme.mcgill.ca/sw/) was used to perform image segmentation and to specify the material properties, the boundary conditions and the mechanical loads. Two complete FE models have been built based on the microCT data for ears 2017-1 and 2017-2 (Figure 3a&b) in addition to the one built

previously [34] for ear 2016-1 (Figure 3c). The original format of the microCT data is individual DICOM files. This format was converted to a format that Fie can recognize (i.e., 8-bit TIFF, JPEG or PNG). The original DICOM images have 16 bits/channel, so we examined the histograms and determined a good grey-level range to reduce the pixel data down to 8 bits/channel (i.e., 8 bits/pixel for grey-level images, which have a single channel). ImageMagick (https://imagemagick.org/) was used to reduce the number of bits and to convert DICOM files to JPEG. The value of 95 for quality (which has a maximum value of 100) was used to specify the amount of lossy JPEG compression.

We segmented the microCT images manually in each slice. The Tr3 program was then used for the generation of triangulated surfaces, and the volume mesh generation was done with Gmsh [36]. Fad was used to join the different structures to produce a final mesh representing all parts of the model. The models contained the following separate structures: pars tensa (PT) of the TM, pars flaccida (PF) of the TM, TM-malleus connection (TMMC), malleus, incus, stapes, incudomallear joint (IMJ), and incudostapedial joint (ISJ) (Figure 2). The IMJ was included only in the models for ears 2017-1 and 2017-2. Histological images of human ears were used as a supplement during modelling because the soft-tissue contrast of the microCT images was inadequate for image segmentation of soft-tissue structures.

For FE analysis we used Salome-Meca V2017.0.2, which integrates Code_Aster 13.4 and astk 2017.0 (http://www.code-aster.org/). We used this old version because newer versions could not be used remotely. The astk tool is used to run Python command files and link all input and output files together to run simulations. Salome-Meca provides integration of the Code_Aster solver with Salome (https://www.salome-platform.org), a generic pre- and post-processor for numerical simulations. Simulation results can be analyzed extensively in the ParaVis module that represents the integration of ParaView (https://www.paraview.org/) into Salome-Meca. The results can be analyzed graphically and also analytically via the Python shell embedded in ParaVis.

Specifying a uniform sound pressure of 2 $Pa_{0\text{-}p}$ at the TM, we computed the frequency response of the system over a frequency range of 100 Hz to 10 kHz for 500 consecutive frequencies. Harmonic analysis was also performed for the frequencies 500 Hz, 1 kHz and 2 kHz, so that we can compare the simulation results with the OCT measurements, which were made at those three frequencies and at that sound pressure level. Simulations were done on an Intel Core i7-4790 CPU with 8 GB RAM and Ubuntu Linux 18.04. Each simulation for the calculation of the frequency response of the model, with one set of parameters, takes between 0.8 and 8.5 minutes, depending on the model. Sensitivity analysis (coded in Python) was performed on the same system.

Specifications of FE models

The TM was represented by a single layer of shell elements, with uniform thickness within the PT and within the PF. The TM boundary was assumed to be fully clamped. The ear canal was not modelled. The anterior mallear ligament and the posterior incudal ligament were also not modelled. Instead, three very stiff orthogonal springs, each having a stiffness of 1000 N/m, were attached to a node at each of those ligaments' locations, effectively fixing those nodes for translation but not for rotation. The annular ligament of the stapes was modelled with springs located at four different nodes on the stapes footplate and approximately perpendicular to the footplate. The baseline stiffness of each of the springs was set to 50 N/m. This is based on the experimental measurement of the stiffness of the annular ligament by Kwacz et al. [37]. They used atomic force microscopy to measure the elastic properties of the annular ligaments in two cadavers. The cochlear load was modelled with four dashpot elements perpendicular to the stapes footplate. The baseline damping coefficient was taken to be 0.2 Ns/m [7, 10] divided among the four dashpots. As displacements occurring in the middle ear in

response to a 2-Pa sound pressure are small, linear material properties (isotropic Young's modulus and Poisson ratio) were defined for each structure of the middle ear separately. Linear (first-order) elements were used in the FE modelling. For the TM, triangle shell elements were used, and the rest of the model was made of 3D tetrahedron elements, except for the springs and the dashpots which were modelled as discrete elements. Each unconstrained node of a shell element has six DOFs: three translational (x, y and z) and three rotational (around x, y and z). In contrast, each unconstrained node in a 3-D solid element has only three DOFs, all of them translational.

Table 1 shows the base material properties we used for different structures of the middle ear [18]. The third column of the table shows other sources that had used these same values before De Greef et al. [18]. The Young's moduli of the PT and PF were decreased for 2017-1 and 2017-2, but not for 2016-1, from the base value to half that value because otherwise the TM was too stiff. For all structures we considered uniform material properties. For the ossicles, a loss ratio of 0.01 was used. For the PT, PF, TMMC and the joints, a loss ratio of 0.2 [38] was used. A Poisson ratio = 0.3 was used for the ossicles and a value of 0.49 was used for the soft tissues.

Mesh convergence analysis

A coarse FE mesh is computationally less expensive than a fine mesh, but the results may not be accurate enough. A systematic mesh convergence analysis should be done to choose an appropriate mesh resolution. We performed mesh convergence tests using the Homard tool in Salome-Meca. We bisected the elements of the soft structures (TM, IMJ, ISJ, TMMC) from the initial mesh three times and calculated the percentage difference between the displacement results for three specific nodes in the model: one node on the posterior PT (PPT) of the TM, one node at the umbo and one node at the middle of the stapes footplate. We plotted the displacement magnitudes of the frequency response after each model refinement. We considered the low-frequency displacement magnitude and the first and second resonance frequencies and concluded that the results had converged if the changes were less than 5%. Based on this criterion, we used the model with no refinement of the TM, with the IMJ and the TMMC being refined once and with the ISJ being refined twice. The model definitions can be found on-line [39].

Parameter sensitivity analysis

After assigning baseline material properties of the models, the material parameters were increased and decreased, one parameter at a time, by factors of 1.5 and 3 from their baseline values. We chose two factors because we wanted to check a wide range of parameter values and we also wanted to know if the changes are linear or not. We simulated the model behaviour and calculated the frequency responses of the models as the parameters changed, and then we quantified the changes between the frequency-response results for each scenario.

Comparison of OCT and model results

For the TM spatial vibration pattern, quantitative comparison of the simulation results and the OCT vibration measurements was done by comparing the presence of maximum displacements in three parts of the TM: PF, PPT and anterior PT (APT). Both relative magnitudes and the numbers of maxima were considered during the comparison. For the models we used the displacement maps and considered

a point to be a local maximum if its displacement was at least twice as high as the displacements of the points at the nearest minima. The OCT data are very noisy and we needed to watch the vibration animations (produced by the Animator software) from different angles to locate the manubrium and different parts of the TM, incus and stapes and to find the maximum displacements and the phases on the TM. After locating the maxima, we marked them on the screenshots of the vibration maps of the TM using Inkscape (https://inkscape.org/). These marked-up images of the TM vibration patterns can be compared with the corresponding simulated displacement magnitude patterns of the TM. The displacement magnitudes of five points (one on the PPT, one on the APT, one at the umbo, one on the long process of the incus and one on the stapes) were also compared one by one between the OCT measurements and the models for different frequencies.

RESULTS

Frequency responses

Figure 4 shows frequency responses from our three FE models, for the umbo (panel a) and stapes footplate (panel b), along with both model results and experimental data from the literature. The experimental data include those of Gyo et al. [40] (one ear, as reported by Koike et al. [41]), Gan et al. [7] (ranges reported for ten ears) and Cheng et al. [42] (four individual ears), all measured in cadaveric temporal bones. The results obtained by FE analysis are from Sun et al. [43], Koike et al. [41] and Gan et al. [7]. The models are different from one another by up to a factor of 20. The results of the models from previous studies shown in Figure 4 lacked peaks and valleys over the frequency range, which may have been due to low frequency resolution or heavy damping or both. The experimental data show more peaks and valleys and they are very different between individual bones and between the groups. For the umbo, the displacements for our models fall within the range of the previous experimental and modelling results at frequencies lower than about 2 kHz but are lower at higher frequencies. For the stapes, the displacements of our models are higher than the experimental data below 1 kHz but they are still within the range of the values of the previous models. Our models have differences among themselves of up to a factor of 2 at lower frequencies and even more at higher frequencies.

Comparison of OCT measurements and simulation results

In Figures 5 to 7 the left panels show the TM vibration patterns extracted from the experimental OCT measurements for frequencies of 500 Hz, 1 kHz and 2 kHz, and the right panels show the simulation results for the base models for the three ears at the same frequencies. The orange line on an OCT image represents the canal wall while the cyan line represents the TM boundary, with a dashed line indicating the part that is hidden by the canal wall. There was a smaller field-of-view during the recording for ear 2016-1, which results in seeing only a portion of the TM. Maxima are shown by black closed lines. The phases of the vibrations of the ears were estimated from the animations of these data (see example animation on-line [39]). If the phase of a local maximum is different from the phase of the global PT maximum by about 180°, it is shown with a dashed line. If the phase is different by about 90° it is shown with a dotted-dashed line. Locations that in the animations appear to correspond to travelling waves are shown by dotted lines. We see artifacts (with the centres of two maxima on the PT being blue instead of yellow) in the OCT data of ear 2017-1 at 1 kHz, because the TM vibration levels in those regions exceeded one half of the optical wavelength of 1550 nm, causing the phase-unwrapping algorithm to break down.

For all three bones at 500 Hz, the simulated vibration pattern has a global maximum on the PPT and a broad maximum on the APT, and the displacements in different parts of the TM are all in phase. In the OCT data also we see the global maximum on the PPT. For the OCT data of ears 2017-1 and 2017-2 we see three maxima, including the global maximum and two smaller maxima on the PPT. For the OCT data of 2017-1 and 2017-2 there is one local maximum on the APT with a magnitude of about half of the global maximum. For the OCT data of ear 2016-1, only a small part of the APT was recorded because the field of view was limited, but there was a low broad maximum that can be seen in the superior part of the APT.

At 1 kHz there are one large maximum and two smaller maxima on the PPT in the models for both 2017-1 and 2017-2. For the OCT data of 2017-1 we see two maxima on the PPT which have similar magnitudes but different phases. For the OCT data of 2017-2 there is one global maximum on the PPT and three smaller local maxima that have different phases. The OCT data for both ears show a relatively low-amplitude local maximum on the APT which is not seen in the simulation results, where the displacements on the APT are very small, with no evident maximum.

At 2 kHz there are three local maxima on the PPT of the 2017-1 model, and the 2017-2 model has four maxima. There are three local maxima on the APT of the 2017-1 model while 2017-2 has four maxima. Both the 2017-1 and 2017-2 models show one maximum on the PF. The magnitudes of the APT and PPT maxima of ear 2017-2 are close in value, for both the model and the OCT, but for ear 2017-1 the maxima on the PPT have higher magnitudes, for both the model and the OCT.

In Figure 8, panels a, b and c show the displacement magnitudes for five locations estimated from the OCT measurements for all three ears, along with the displacement magnitudes for the models at the same frequencies. For the OCT data we selected the locations that show the maximum displacements in the PPT and in the APT. In addition, we considered the umbo, long process of incus, and stapes, whose locations were estimated as described in Methods. For the model, we chose four fixed nodes (in the middle of the APT, at the umbo, on the long process of the incus, and on the stapes head) that correspond to the OCT locations at which we measured. (The displacements are about 2% higher at the stapes head than at the footplate for frequencies below 2 kHz.) For the PPT, however, since the models all had distinct maxima but at different locations, we selected the model node with the maximum displacement rather than using a fixed node. The experimental measurements at different frequencies were done separately and there was uncertainty about the sound pressure value at the TM in some cases, possibly because of the leaks in the sound system. Therefore, for this figure, at each frequency the OCT measurements for the umbo were scaled so that they had the same displacement magnitude as in the model, and then the OCT measurements for the other locations were adjusted by the same scale factor. In Figure 8, some of the differences between the model displacements and the corresponding OCT displacements are quite large, especially for the PPT. We scaled the OCT results based only on the umbo displacements because the OCT results are less noisy at the umbo than at the deeper locations. If we instead scaled the OCT curves to give the best overall match to the model results at all locations, the differences between the OCT and model results would appear smaller. Either way, most of the differences seen here are probably smaller than the displacement changes that are caused by some pathological middle-ear conditions. Figure 8 shows that the displacements for PPT, incus and stapes are always larger in the model. The results for the models have maximum differences from the scaled OCT results of between 1.2 dB and 3.6 dB for different ears on the PPT for frequencies of 500 Hz and 1 kHz and the differences become as large as 11.6 dB at 2 kHz in ear 2017-2. The incus and stapes have similar magnitudes for both OCT and the models except for the OCT data for ear 2017-2, where the stapes displacements are smaller. The umbo-to-incus magnitude ratio is mostly about twice as high for OCT but at 2 kHz for ear 2017-2 the ratio is about five times as high for OCT. The

magnitude of the APT displacement is sometimes estimated well by the model but in some cases there is a difference of about a factor of 10 between the model and OCT.

Parameter sensitivity analysis

A parameter sensitivity analysis was done to see how changing parameter values affects the model behaviour. This helps us to understand which model parameters are most responsible for various features of a model's output, and can give hints on how to improve the model by adjusting the parameters. Figure 9 shows the results of increasing and decreasing the parameters for the model of ear 2017-2 by factors of 1.5 and 3. Panels a to c represent changes of low-frequency displacement magnitude for the PT, umbo and stapes, and panel d shows changes of the PT resonance frequency. The horizontal positions of the different values for each parameter are located at the values 0.33, 0.67, 1, 1.5 and 3 on locally linear scales, where 1 corresponds to the base value of the parameter and the other values represent the scaling of the parameter. The results were qualitatively and quantitatively similar for the other ears. From Figure 9 we see that the thickness and Young's modulus of the PT have significant effects on the low-frequency displacement values of the middle ear on the TM and ossicles. Displacements on the ossicles are also affected by the stiffness of the annular ligament and the cochlear impedance. The Young's modulus of the TMMC and IMJ have negligible effects and the Young's modulus of the ISJ changes the results only for the ossicles. The changes of the displacement magnitude and resonance frequency were not always linear when parameter values were changed. Details of the non-linearities are discussed below for some parameters.

Further details of Figure 9 will be discussed below in the context of Figures 10 to 17, which show the complete frequency responses for parameter increases and decreases. The results are again qualitatively and quantitatively similar among the ears so we only present the figures for ear 2017-2. In the following sections we discuss the results for different parameters. The displacements ($nm_{0\text{-}p}$) correspond to an applied pressure of 2 $Pa_{0\text{-}p}$.

Thickness and Young's modulus of pars tensa

In Figures 10 and 11 we see that the frequency response curves for the umbo and stapes shift downward for increasing PT thickness and Young's modulus for frequencies below about 1 kHz. The curves also shift to higher frequencies as both the PT thickness and Young's modulus increase, causing displacement increases for frequencies above about 1 kHz.

Figure 9 shows that increasing the thickness of the PT by a factor of 1.5 will decrease the low-frequency displacement magnitude of the PT by about 50%, and decreasing it by the same factor will increase the displacement by about 100%. This is true for all three ears. The effects are smaller at the ossicles. The umbo and stapes displacement magnitudes change by about 40% for ear 2016-1 and by about 20% for ears 2017-1 and 2017-2. The PT displacement changes are larger when the PT thickness decreases, while the displacement magnitudes of the ossicles change more when the PT thickness increases. If the thickness of PT is increased by a factor of 1.5 it will increase the main resonance frequency of the middle ear by about 20%, and if it is decreased by a factor of 1.5 it will decrease the resonance frequency by about the same amount. Figure 10 shows that the troughs of the frequency response of the PT change dramatically when the PT thickness is changed. We see, from smallest to largest thickness, that the first trough is very rounded, then somewhat rounded, then very sharp, then quite round, and then very sharp again. Presumably this is because of interactions with resonances at other locations on the PT. The number of troughs is greater when the thickness is lower, and when there are more troughs some of them are rounder.

Figure 9 shows that increasing the Young's modulus of the PT by a factor of 1.5 will decrease the low-frequency displacement magnitude of the PT by 30%, and decreasing it by the same factor will increase the displacement by about 50%. Figure 11 shows that increasing the Young's modulus of the PT by a factor of 1.5 shifts the frequency of peaks and valleys to higher frequencies by about 20% for the PT, umbo and stapes. Again, this is true for all three ears. The displacement magnitude changes for the umbo and stapes at lower frequencies are about 20% for ear 2016-1 and 10% for ears 2017-1 and 2017-2. The Young's modulus of the PT has larger effects on the displacement magnitude at higher frequencies on the ossicles while changes due to the PT thickness are more constant across frequencies. When the Young's modulus of the PT is changed, the damping of the PT will also change because we have a constant loss ratio, and this will increase the effect on the displacements at higher frequencies. Changes of the PT thickness have stronger effects on the displacements than changes of the Young's modulus of the PT do.

Cochlear damping

Figure 12 shows the results for different cochlear damping values, again for ear 2017-2. Increasing the cochlear damping beyond the baseline value had practically no effect, but we tested a wider than usual range of values lower than baseline. The motivation was to see whether cochlear damping might be obscuring some resonances of the middle ear. The maximum of the frequency response for the TM is at 1 kHz regardless of the cochlear damping values. At the lowest damping value tested, 0.0125, we see a shoulder or an extremely low peak on the umbo and stapes at 1 kHz for 2017-1 and 2017-2, which presumably reflects the TM peak. We also see a maximum in the umbo and stapes frequency responses at ~600 Hz for ears 2017-1 and 2017-2. For those ears the TM has a small peak close to this ossicular maximum, and there is a minimum in between that and the main maximum, at around 750 Hz. In the model for 2016-1, this ossicular resonance frequency is at ~900 Hz, closer to the main resonance of the PT at 1 kHz, and it is not visible in the PT frequency response even at the lowest level of damping. As the values of the cochlear damping were increased, the first peak became smaller until it disappeared by 0.1. This suggests that some part of the ossicular chain in this model has a resonance frequency at less than 1 kHz which is heavily damped by the cochlear impedance. At frequencies higher than 1 kHz, the TM frequency response does not change with changes in the cochlear damping, while minima and maxima in the frequency responses of the umbo and stapes become sharper with the decreased cochlear damping.

Soft tissues: incudomallear joint, incudostapedial joint and TM-malleus connection

In Figures 13 and 14 we see that the Young's modulus of the IMJ and ISJ do not have any noticeable effect on the TM frequency response and they have small effects on the umbo and stapes frequency responses. For the IMJ, the resonance frequency and the displacement magnitude at frequencies below 2 kHz change by less than 5%, but we see larger changes in the magnitude at higher frequencies. The Young's modulus of the ISJ changes the frequency response between 1 and 4 kHz at the umbo and stapes and at other frequencies the effect is less than 5%. A trough on the stapes frequency response shifts from about 2 kHz to about 3.4 kHz when the Young's modulus of the ISJ is increased and the trough also becomes deeper.

Figure 15 shows the effects of damping of the ISJ on the models. The figures contain two situations: the baseline loss ratio of 0.2 and a lightly damped ISJ with a loss ratio of 0.01. We see that when the damping is very light a sharp peak and one or two sharp valleys appear between 3 and 5 kHz for both umbo and stapes. The features essentially disappear for the baseline value of damping. There is a similar pattern for ear 2016-1 but the model for ear 2017-1 does not have these features. The stapes is

tilted with respect to the TM in ear 2017-1 and the footplate is displaced in the oval window, which may be why these features are not present in this ear. As mentioned above, ear 2017-1 is also more sensitive to decreases of the Young's modulus of the IMJ.

Varying the Young's modulus of the TMMC over the range of 0.66 to 6 MPa caused changes of less than 2% in the TM, umbo and stapes displacements.

Stiffness of stapedial annular ligament

Figure 16 shows that the stiffness of the stapedial annular ligament changes the PT displacements by less than 3% in ear 2017-2, and the same is true in the other two ears. Changes in the frequency response of the umbo and stapes for a change by factor of 1.5 are about 10% for ear 2016-1 and about 20% for ears 2017-1 and 2017-2.

Loss ratio

Figure 17 shows that increasing the loss ratio will decrease the magnitudes of the peaks of the frequency response of the PT and ossicles. Note, however, that minima for the PT are deepest at the baseline value of damping and either increasing or decreasing the loss ratio makes the minima less deep. Changing the damping did not noticeably shift the resonance frequency.

DISCUSSION

In this study we modelled three cadaveric human middle ears. We were able to compare the models to the OCT measurements in terms of the TM displacement patterns and also the displacement values extracted from the OCT data for the umbo, incus and stapes. The TM displacement patterns from the simulations are qualitatively similar to the OCT measurement data for the three ears, as described for Figures 5 to 7. Figure 8 shows the measured and simulated displacement magnitudes for the different locations in each ear. The figure shows that, for the locations considered, the displacement values of the models are closest to the OCT measurements at 500 Hz and the difference is greatest at 2 kHz. As in all middle-ear modelling, at around 1 kHz significant discrepancies between experimental and model responses can arise from relatively small differences in the main middle-ear resonance frequency, and at higher frequencies significant discrepancies can arise from small differences in the complex spatial patterns.

As described in Methods, ears 2017-1 and 2017-2 were the left and right ears of the same individual. These ears were similar in size but the orientation of the stapes with respect to the TM was different between the two ears. Because the middle ear space was not violated during the dissection, we believe that the difference in stapes location was most likely due to a pathological condition or a congenital abnormality of the ear rather than being an artefact of its preparation. In general there is considerable variability among ears [e.g., 11–13, 15], especially in the stapes [e.g., 44]. Ear 2016-1 was about 10% larger in size in all directions than ears 2017-1 and 2017-2. Ear 2016-1 belonged to a person 170 cm in height while ears 2017-1 and 2017-2 belonged to a person 183 cm in height. The ear size was not proportionate to the height of the individual, which is not surprising given the variability between people not only in size but in shape and proportions.

Having multiple models helped us in evaluating the relationship between the shape and behaviour of the models. The models have different frequency responses that vary by up to a factor of 2 at low frequencies and they are more different at higher frequencies (Figure 4). The baseline material properties were the same except for the Young's modulus of the TM, which was made twice as high in the 2016-1 model as discussed in Methods. As described in Results, the three models respond similarly

to changes of the parameters. Based on the geometries of the three ears we had, the results of the parameter sensitivity analysis are very similar among the three ears. Only the sensitivity to ISJ damping was different from the others in ear 2017-1, in which the stapes had a different orientation. If we want to make general claims about how geometry and size of different parts of the middle ear will affect the model behaviour, we will need to have more samples. We did not test the sensitivity of the models to changes of the shapes and dimensions of the structures, but this has been done in a few previous studies. Funnell and Laszlo [1] looked at the effects of the TM shape by varying geometric parameters in a cat eardrum model and they concluded that the curvature and conical shape of the TM are important. Moiré shape measurement was used by Funnell and Decraemer [16] to build individualized FE models for four different animal ears, and the effects of the variability were examined. They also scaled the TM boundary by 5%, which changed the TM displacements by 4–15%. Koike et al. [17] analyzed three models with different depths of the TM and found that the transmission factor changed by about 5 dB if the depth was changed by a factor of 2. Motallebzadeh et al. [10] provided an estimate of the effects of anatomical variability by varying the size of their model by ±5% and ±10% in the x, y and z directions separately and also in all three directions simultaneously, which changed the results by up to 50% for 10% changes. De Greef et al. [18] concluded that the influence of different shapes of the TMMC (whether narrow or wide) was limited to 2.3 dB.

From the parameter sensitivity analysis we found that the parameters of the model that affected its behaviour the most were the PT thickness and the Young's modulus of the PT. This is in agreement with previous studies [e.g., 6, 7, 10].The influence of the value of the annular-ligament stiffness was large, which is also in agreement with previous studies [e.g., 6, 18]. The fact that the results are sensitive to such parameters suggests that ear-specific modelling may be required for each patient. While material properties would be difficult to measure for each ear and may require parameter fitting, TM thickness may be determined from OCT [24, 25, 45]. As previous studies have also found, the damping coefficients of the TM and soft tissues are also important [e.g., 10, 18, 41]. Values of the viscous cochlear damping had a large effect on the stapes displacements, which is in agreement with previous studies [e.g., 7, 18]. We found that it also has an effect on the number of resonances seen on the TM if the value for the damping is unrealistically low (Figure 12), as described in Results, which could give some insight into the individual resonating structures in the middle ear, whose resonances are usually indistinguishable.

There were various assumptions in our modelling. The PT thickness was considered uniform, but in reality the PT has a non-uniform thickness as was measured in previous studies [e.g., 24, 46, 47]. Some studies have modelled a nonuniform thickness for the human TM [4, 18, 41, 43], but most have assumed a uniform thickness, even if this parameter is considered to have a strong effect on the model results [e.g., 48]. Isotropy was considered here for the TM because there is no strong direct evidence for functional anisotropy [e.g., 49]. De Greef et al. [18] used both isotropic and orthotropic material properties for the TM in their models and concluded that the results had differences of less than 3.3 dB over the frequency range of 0.1 to 10 kHz, and the vibration patterns of the TM were similar for the two types of model.

The IMJ was not considered in the creation of the model for ear 2016-1 and therefore the model had about 10 times fewer elements and was computationally much less expensive (about 10 times faster). The IMJ is wide and thin and its shape is such that we need to have many elements to have an acceptable aspect ratio for the elements. In our parameter sensitivity analysis it was found that the IMJ Young's modulus changed the resonance frequency and the displacement magnitude for frequencies up to 2 kHz by less than 5 percent. Increasing the IMJ Young's modulus to that of bone had negligible effects, and decreasing it by a factor of ten below baseline changed the displacement magnitudes up to 2 kHz by only about a factor of 4 or less. Considering the fact that modelling the IMJ is very time

consuming because of its rather complex saddle shape and the great uncertainty of its boundaries in the microCT images, we suggest that, at least for frequencies up to 2 kHz, the ear can be modelled without the IMJ and with the incus and malleus having a shared surface, to have a less computationally expensive model. Hoffstetter et al. [50] also reported that the Young's modulus of the IMJ did not significantly change the results of their FE model of the human middle ear, but there are some contradictory experimental data [51, 52]. The coupling between the incus and the stapes, on the other hand, can be expected to be important because it converts the largely rotational movements of the malleus and incus to the largely piston-like movements of the stapes. In our parameter sensitivity analysis the Young's modulus and damping of the ISJ both changed the shape of the frequency response, mostly between 1 kHz and 4 kHz (Figures 14 and 15), and this is in agreement with previous studies [e.g., 4, 7, 17, 18]. The Young's modulus of the TMMC was reported to be influential by Hoffstetter et al. [50] and De Greef et al. [18] but we found it to have an effect of less than 2%, which is in agreement with Koike et al. [41].

Although we have computed frequency responses up to 10 kHz for the three models, the frequency of the OCT data here is limited to 500 Hz, 1 kHz and 2 kHz. We can use 500-Hz OCT data to represent frequencies lower than that because the frequency response is rather flat at such frequencies. The middle ear's main resonance frequency is close to 1 kHz, which is a disadvantage of using 1 kHz to characterize an ear because the displacement magnitudes will be affected by any shift of the resonance. The TM is reported to start having complex vibration patterns at 2 kHz [e.g., 32], which makes 2 kHz useful for checking whether we see the same trend or not.

A drawback of the OCT volume measurement is the long time needed for each data recording. For this reason OCT measurements were made at a limited number of frequencies. If we used point measurements, they could be obtained at a much faster rate and having more frequencies would be feasible. If a FE model could be validated using OCT data for more frequencies, we could better infer how the ear was functioning at other frequencies.

Our OCT data for the incus and stapes are limited for the purpose of investigating their motions because we only see the vibrations of the long process of the incus and part of the stapes, and only the vibration component in the direction of the laser beam (which is approximately parallel to the axis of the ear canal and to the piston direction of the stapes) is measured. The model displacements here were measured in the same direction.

Figure 4 shows that the frequency responses of our models fall faster at high frequencies than the experimental data do. We think this might be because of the way energy dissipation is modelled and/or because of modelling the TM as isotropic [53], and/or because of not modelling the suspensory ligaments. Because our models were compared to OCT measurements that were only up to 2 kHz, we did not attempt to address this issue.

In this study three FE models were validated with their own OCT vibration data at three different frequencies. Parameter sensitivity analysis results were compared among the models and with the literature. In the future it will also be possible to build models in which pathological conditions are simulated, such as stapes fixation and ISJ interruption. MicroCT imaging of patients would not be possible and, while real-time volumetric OCT B-mode acquisition has already been demonstrated in patients [29], further advances in middle-ear OCT technology will be needed to enable acquisition of volumetric Doppler OCT data in a clinically feasible acquisition time. The geometries of the existing FE models could be modified for the new patients based on clinical CT images. The OCT values at the measured points could be compared with the simulation results of the new model. Parameters of the new model could be adjusted to fit the measurements and might be able to identify abnormalities in the middle ear.

Table 1 Baseline material properties

Structures	Baseline values	Sources
Eardrum		
Mass density (kg/m^3)	1200	[54]
Young's modulus (MPa)		
PT	20	
PF	6.7	
Malleus		
Mass density (kg/m^3)	2550	[55 pp. 87-94]
Young's modulus (GPa)	1.41	[56]
Incus		
Mass density (kg/m^3)	2360	[55 pp. 87-94]
Young's modulus (GPa)	1.41	[56]
Stapes		
Mass density (kg/m^3)	2200	[55 pp. 87-94]
Young's modulus (GPa)	1.41	[56]
ISJ		
Mass density (kg/m^3)	1200	[43]
Young's modulus (MPa)	6	[41]
IMJ		
Mass density (kg/m^3)	1200	[43]
Young's modulus (MPa)	7	[57]
TMMC		
Mass density (kg/m^3)	1200	[43]
Young's modulus (MPa)	2	

REFERENCES

1. Funnell WRJ, Laszlo CA (1978) Modeling of the cat eardrum as a thin shell using the finite-element method. J Acoust Soc Am 63:1461–1467. https://doi.org/10.1121/1.381892

2. Wada H, Metoki T, Kobayashi T (1992) Analysis of dynamic behavior of human middle ear using a finite-element method. J Acoust Soc Am 92:3157–3168. https://doi.org/10.1121/1.404211

3. Beer HJ, Bornitz M, Hardtke HJ, Schmidt R, Hofmann G, Vogel U, Zahnert T, Hüttenbrink KB (1999) Modelling of components of the human middle ear and simulation of their dynamic behaviour. Audiol Neurootol 4:156–162. https://doi.org/10.1159/000013835

4. Prendergast PJ, Ferris P, Rice HJ, Blayney AW (1999) Vibro-acoustic modelling of the outer and middle ear using the finite-element method. Audiol Neurotol 4:185–191. https://doi.org/10.1159/000013839

5. Daniel SJ, Funnell WR, Zeitouni AG, Schloss MD, Rappaport J (2001) Clinical applications of a finite-element model of the human middle ear. J Otolaryngol 30:340–346. https://doi.org/10.2310/7070.2001.19393

6. Mikhael CS, Funnell WRJ, Bance M (2004) Middle-ear finite-element modelling with realistic geometry and apriori material- property estimates. Proc 28th Ann Conf Can Med Biol Eng Soc

7. Gan RZ, Feng B, Sun Q (2004) Three-dimensional finite element modeling of human ear for sound transmission. Ann Biomed Eng 32:847–859. https://doi.org/10.1023/B:ABME.0000030260.22737.53

8. Zhao F, Koike T, Wang J, Sienz H, Meredith R (2009) Finite element analysis of the middle ear transfer functions and related pathologies. Med Eng Phys 31:907–916. https://doi.org/10.1016/j.medengphy.2009.06.009

9. Zhang X, Guan X, Nakmali D, Palan V, Pineda M, Gan RZ (2014) Experimental and modeling study of human tympanic membrane motion in the presence of middle ear liquid. J Assoc Res Otolaryngol JARO 15:867–881. https://doi.org/10.1007/s10162-014-0482-8

10. Motallebzadeh H, Maftoon N, Pitaro J, Funnell WRJ, Daniel SJ (2017) Finite-element modelling of the acoustic input admittance of the newborn ear canal and middle ear. J Assoc Res Otolaryngol JARO 18:25–48. https://doi.org/10.1007/s10162-016-0587-3

11. Todd NW (2005) Orientation of the manubrium mallei: inexplicably widely variable. The Laryngoscope 115:1548–1552. https://doi.org/10.1097/01.mlg.0000173171.32899.4e

12. Todd NW (2007) Pars flaccida retraction and mastoid size: relationship in clinically normal specimens. J Laryngol Otol 121:1020–1024. https://doi.org/10.1017/S0022215107006305

13. Todd NW (2008) The malleus-stapes offset. The Laryngoscope 118:110–115. https://doi.org/10.1097/MLG.0b013e318155a299

14. Bradshaw AP, Curthoys IS, Todd MJ, Magnussen JS, Taubman DS, Aw ST, Halmagyi GM (2010) A mathematical model of human semicircular canal geometry: a new basis for interpreting vestibular physiology. J Assoc Res Otolaryngol JARO 11:145–159. https://doi.org/10.1007/s10162-009-0195-6

15. Todd NW, Daraei P (2014) Morphologic variations of clinically normal mallei and incudes. Ann Otol Rhinol Laryngol 123:461–467. https://doi.org/10.1177/0003489414527228

16. Funnell WRJ, Decraemer WF (1996) On the incorporation of moiré shape measurements in finite-element models of the cat eardrum. J Acoust Soc Am 100:925–932. https://doi.org/10.1121/1.416252

17. Koike T, Wada H, Kobayashi T (2001) Effect of depth of conical-shaped tympanic membrane on middle-ear sound transmission. JSME Int J Ser C-Mech Syst Mach Elem Manuf. https://doi.org/10.1299/JSMEC.44.1097

18. De Greef D, Pires F, Dirckx JJJ (2017) Effects of model definitions and parameter values in finite element modeling of human middle ear mechanics. Hear Res 344:195–206. https://doi.org/10.1016/j.heares.2016.11.011

19. Ramier A, Rosowski J, Yun S-H (2018) Optical coherence tomography for imaging the middle and inner ears: A technical review. St Catharines, Canada, p 020001

20. Pitris C, Saunders KT, Fujimoto JG, Brezinski ME (2001) High-resolution imaging of the middle ear with optical coherence tomography: a feasibility study. Arch Otolaryngol Head Neck Surg 127:637–642. https://doi.org/10.1001/archotol.127.6.637

21. Heermann R, Hauger C, Issing PR, Lenarz T (2002) Erste Anwendungen der optischen Kohärenztomographie (OCT) in der Mittelohrchirurgie. Laryngo-Rhino-Otol 81:400–405. https://doi.org/10.1055/s-2002-32213

22. Djalilian HR, Ridgway J, Tam M, Sepehr A, Chen Z, Wong BJF (2008) Imaging the human tympanic membrane using optical coherence tomography in vivo: Otol Neurotol 29:1091–1094. https://doi.org/10.1097/MAO.0b013e31818a08ce

23. Just T, Lankenau E, Hüttmann G, Pau HW (2009) Optische Kohärenztomographie in der Mittelohrchirurgie. HNO 57:421–427. https://doi.org/10.1007/s00106-009-1907-2

24. Van der Jeught S, Dirckx JJJ, Aerts JRM, Bradu A, Podoleanu AG, Buytaert JAN (2013) Full-field thickness distribution of human tympanic membrane obtained with optical coherence tomography. JARO 14:483–494. https://doi.org/10.1007/s10162-013-0394-z

25. Hubler Z, Shemonski ND, Shelton RL, Monroy GL, Nolan RM, Boppart SA (2015) Real-time automated thickness measurement of the in vivo human tympanic membrane using optical coherence tomography. Quant Imaging Med Surg 5:69–77. https://doi.org/10.3978/j.issn.2223-4292.2014.11.32

26. Subhash M, Wang R (2013) Optical coherence tomography: Technical aspects. In: Biomedical optical imaging technologies, ISBN 978-3-642-28390-1. Springer-Verlag Berlin Heidelberg, 2013. pp 163–212

27. Chang EW, Cheng JT, Röösli C, Kobler JB, Rosowski JJ, Yun SH (2013) Simultaneous 3D imaging of sound-induced motions of the tympanic membrane and middle ear ossicles. Hear Res 304:49–56. https://doi.org/10.1016/j.heares.2013.06.006

28. Park J, Carbajal EF, Chen X, Oghalai JS, Applegate BE (2014) Phase-sensitive optical coherence tomography using an Vernier-tuned distributed Bragg reflector swept laser in the mouse middle ear. Opt Lett 39:6233. https://doi.org/10.1364/OL.39.006233

29. MacDougall D, Farrell J, Brown J, Bance M, Adamson R (2016) Long-range, wide-field swept-source optical coherence tomography with GPU accelerated digital lock-in Doppler vibrography for real-time, in vivo middle ear diagnostics. Biomed Opt Express 7:4621. https://doi.org/10.1364/BOE.7.004621

30. Tonndorf J, Khanna SM (1972) Tympanic-membrane vibrations in human cadaver ears studied by time-averaged holography. J Acoust Soc Am 52:1221–1233. https://doi.org/10.1121/1.1913236

31. Cheng JT, Aarnisalo AA, Harrington E, Hernandez-Montes MDS, Furlong C, Merchant SN, Rosowski JJ (2010) Motion of the surface of the human tympanic membrane measured with stroboscopic holography. Hear Res 263:66–77. https://doi.org/10.1016/j.heares.2009.12.024

32. Rosowski J, Cheng J, Merchant S, Harrington E, Furlong C (2011) New data on the motion of the normal and reconstructed tympanic membrane. Otol Neurotol 32:1559–1567. https://doi.org/10.1097/MAO.0b013e31822e94f3

33. Tang H, Psota P, Rosowski JJ, Furlong C, Cheng JT (2021) Analyses of the tympanic membrane impulse response measured with high-speed holography. Hear Res 410:108335. https://doi.org/10.1016/j.heares.2021.108335

34. Wang X (2019) Finite-element modelling of the human middle ear based on X-ray micro-computed tomography and Doppler optical coherence tomography in the same ear. Master’s, McGill University

35. Klein T, Huber R (2017) High-speed OCT light sources and systems. Biomed Opt Express 8:828–859. https://doi.org/10.1364/BOE.8.000828

36. Geuzaine C, Remacle J-F (2009) Gmsh: A 3-D finite element mesh generator with built-in pre- and post-processing facilities. Int J Numer Methods Eng 79:1309–1331. https://doi.org/10.1002/nme.2579

37. Kwacz M, Rymuza Z, Michałowski M, Wysocki J (2015) Elastic properties of the annular ligament of the human stapes--AFM measurement. J Assoc Res Otolaryngol JARO 16:433–446. https://doi.org/10.1007/s10162-015-0525-9

38. Homma K, Du Y, Shimizu Y, Puria S (2009) Ossicular resonance modes of the human middle ear for bone and air conduction. J Acoust Soc Am 125:968–979. https://doi.org/10.1121/1.3056564

39. Funnell WRJ, Golabbakhsh M (2022) Supplementary files for Golabbakhsh et al. (2023). https://borealisdata.ca/dataset.xhtml?persistentId=doi:10.5683/SP3/8BEY4N. Accessed 31 Dec 2022

40. Gyo K, Aritomo H, Goode RL (1987) Measurement of the ossicular vibration ratio in human temporal bones by use of a video measuring system. Acta Otolaryngol (Stockh) 103:87–95. https://doi.org/10.3109/00016488709134702

41. Koike T, Wada H, Kobayashi T (2002) Modeling of the human middle ear using the finite-element method. J Acoust Soc Am 111:1306–1317

42. Cheng JT, Ghanad I, Remenschneider A, Rosowski J (2021) The onset of nonlinear growth of middle-ear responses to high intensity sounds. Hear Res 405:108242. https://doi.org/10.1016/j.heares.2021.108242

43. Sun Q, Gan RZ, Chang K-H, Dormer KJ (2002) Computer-integrated finite element modeling of human middle ear. Biomech Model Mechanobiol 1:109–122. https://doi.org/10.1007/s10237-002-0014-z

44. Coker NJ (1993) Surgical anatomy of the temporal bone. Head&Neck 15:586–587

45. Monroy GL, Shelton RL, Nolan RM, Nguyen CT, Novak MA, Hill MC, McCormick DT, Boppart SA (2015) Noninvasive depth-resolved optical measurements of the tympanic membrane and middle ear for differentiating otitis media. The Laryngoscope 125:E276–E282. https://doi.org/10.1002/lary.25141

46. Kuypers LC, Decraemer WF, Dirckx JJJ (2006) Thickness distribution of fresh and preserved human eardrums measured with confocal microscopy. Otol Neurotol 27:256–264. https://doi.org/10.1097/01.mao.0000187044.73791.92

47. De Greef D, Aernouts J, Aerts J, Cheng JT, Horwitz R, Rosowski JJ, Dirckx JJJ (2014) Viscoelastic properties of the human tympanic membrane studied with stroboscopic holography and finite element modeling. Hear Res 312:69–80. https://doi.org/10.1016/j.heares.2014.03.002

48. Volandri G, Di Puccio F, Forte P, Carmignani C (2011) Biomechanics of the tympanic membrane. J Biomech 44:1219–1236. https://doi.org/10.1016/j.jbiomech.2010.12.023

49. Elkhouri N, Liu H, Funnell WRJ (2006) Low-frequency finite-element modeling of the gerbil middle ear. JARO 7:399–411. https://doi.org/10.1007/s10162-006-0055-6

50. Hoffstetter M, Schardt F, Lenarz T, Wacker S, Wintermantel E (2010) Parameter study on a finite element model of the middle ear. Biomed Tech 55:19–26. https://doi.org/10.1515/bmt.2010.006

51. Willi UB, Ferrazzini MA, Huber AM (2002) The incudo-malleolar joint and sound transmission losses. Hear Res 174:32–44. https://doi.org/10.1016/s0378-5955(02)00632-9

52. Willi UB, Ferrazzini MA, Huber AM Corrigendum to “The incudo-malleolar joint and sound transmission losses” Hearing Research 177 (2002) 123.

53. Motallebzadeh H, Puria S (2021) Mouse middle-ear forward and reverse acoustics. J Acoust Soc Am 149:2711–2731. https://doi.org/10.1121/10.0004218

54. Wada H, Kobayashi T (1990) Dynamical behavior of middle ear: Theoretical study corresponding to measurement results obtained by a newly developed measuring apparatus. J Acoust Soc Am 87:237–245. https://doi.org/10.1121/1.399290

55. Kirikae I (1960) The structure and function of the middle ear. Univ. of Tokyo Press, Tokyo

56. Speirs AD, Hotz MA, Oxland TR, Häusler R, Nolte LP (1999) Biomechanical properties of sterilized human auditory ossicles. J Biomech 32:485–491. https://doi.org/10.1016/s0021-9290(99)00012-3

57. Homma K, Shimizu Y, Kim N, Du Y, Puria S (2010) Effects of ear-canal pressurization on middle-ear bone- and air-conduction responses. Hear Res 263:204–215. https://doi.org/10.1016/j.heares.2009.11.013

Figures

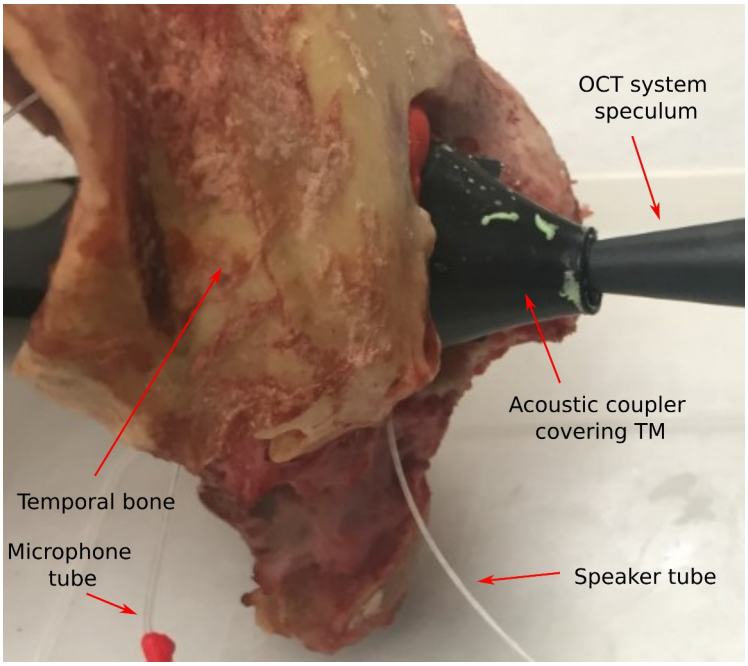

Fig. 1 Setup for OCT measurement in temporal bones

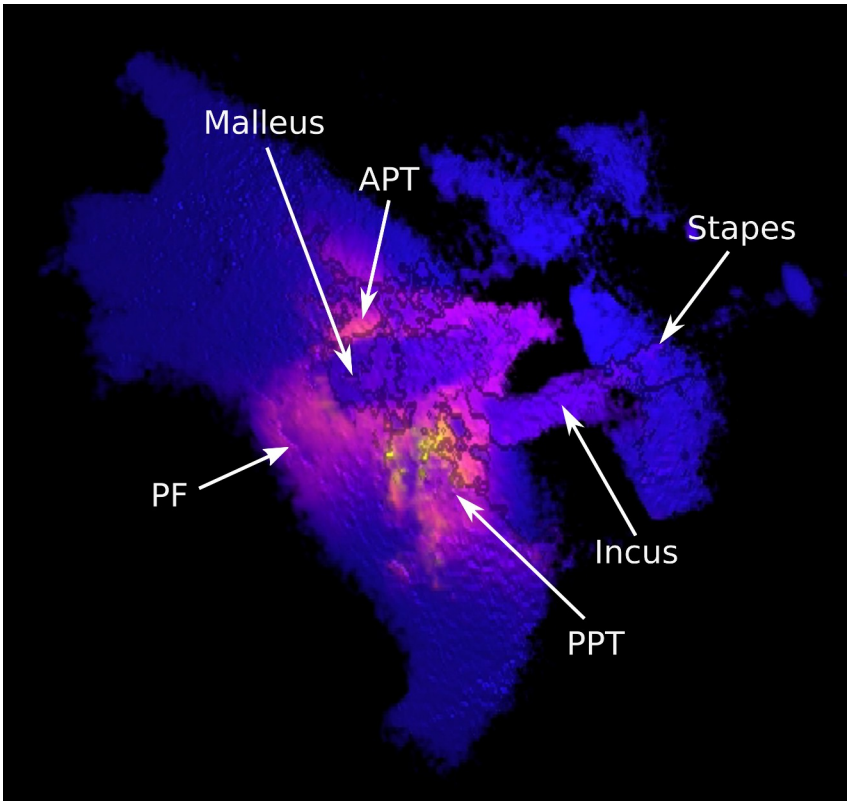

Fig. 2 Volume rendering of OCT measurement of ear 2017-2 at 2 kHz. PPT = posterior pars tensa, APT = anterior pars tensa, PF = pars flaccida

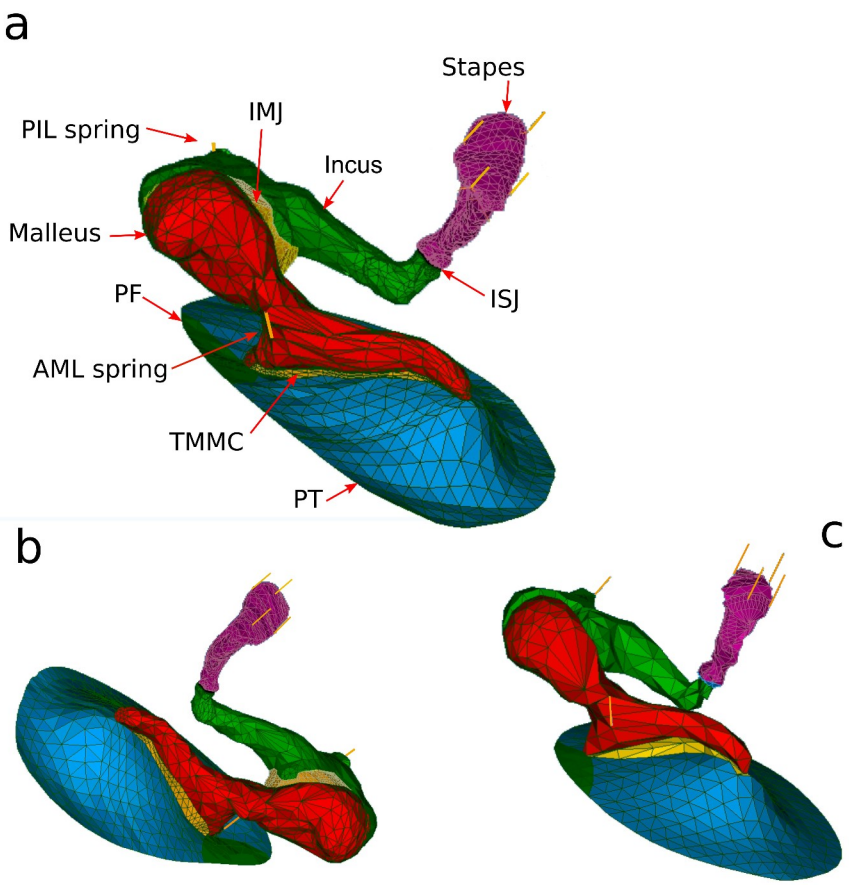

Fig. 3 Finite-element models of three human ears. (a) ear 2017-1, (b) ear 2017-2, (c) ear 2016-1. PPT = posterior pars tensa, APT = anterior pars tensa, PF = pars flaccida, TMMC = TM-malleus connection, AML = anterior mallear ligament, IMJ = incudomallear joint, PIL = posterior incudal ligament, ISJ = incudostapedial joint

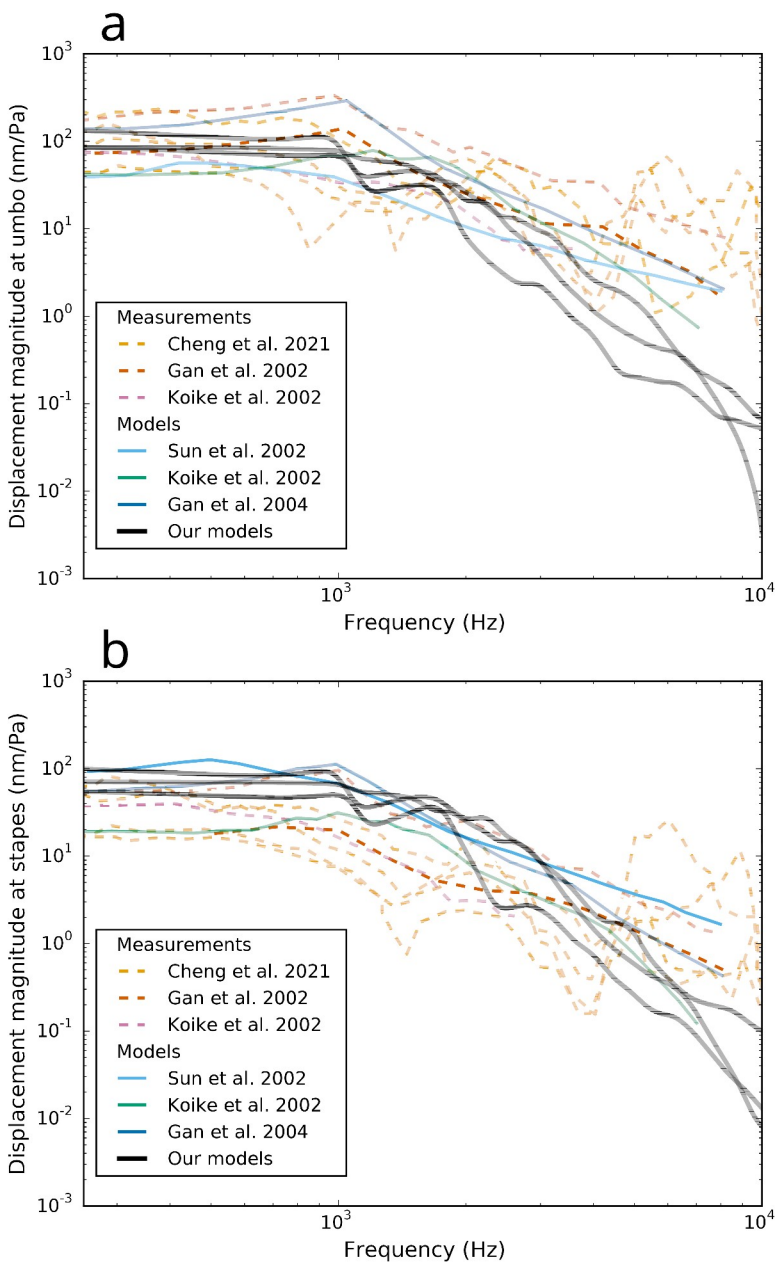

Fig. 4 Comparison of frequency responses of FE models from this study with published experimental data and previous models. (a) at umbo, (b) at stapes

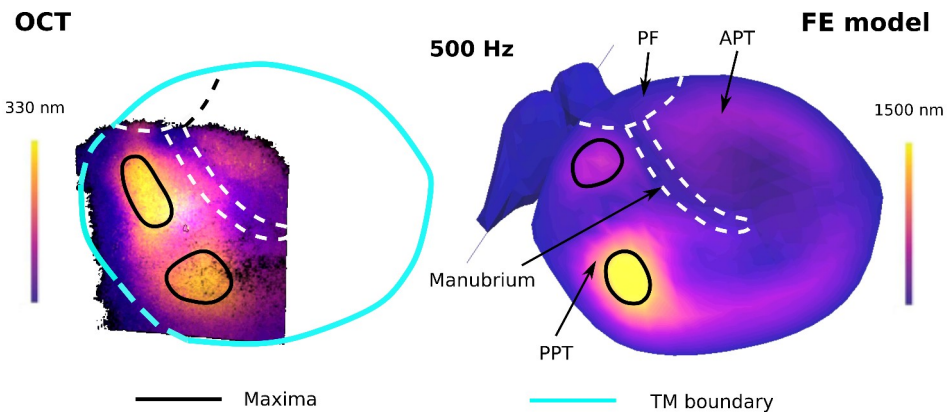

Fig. 5 Vibration displacement maps from OCT measurements and FE simulations at 500 Hz for ear 2016-1. PPT = posterior pars tensa (PT), APT = anterior pars tensa (APT), PF = pars flaccida (PF)

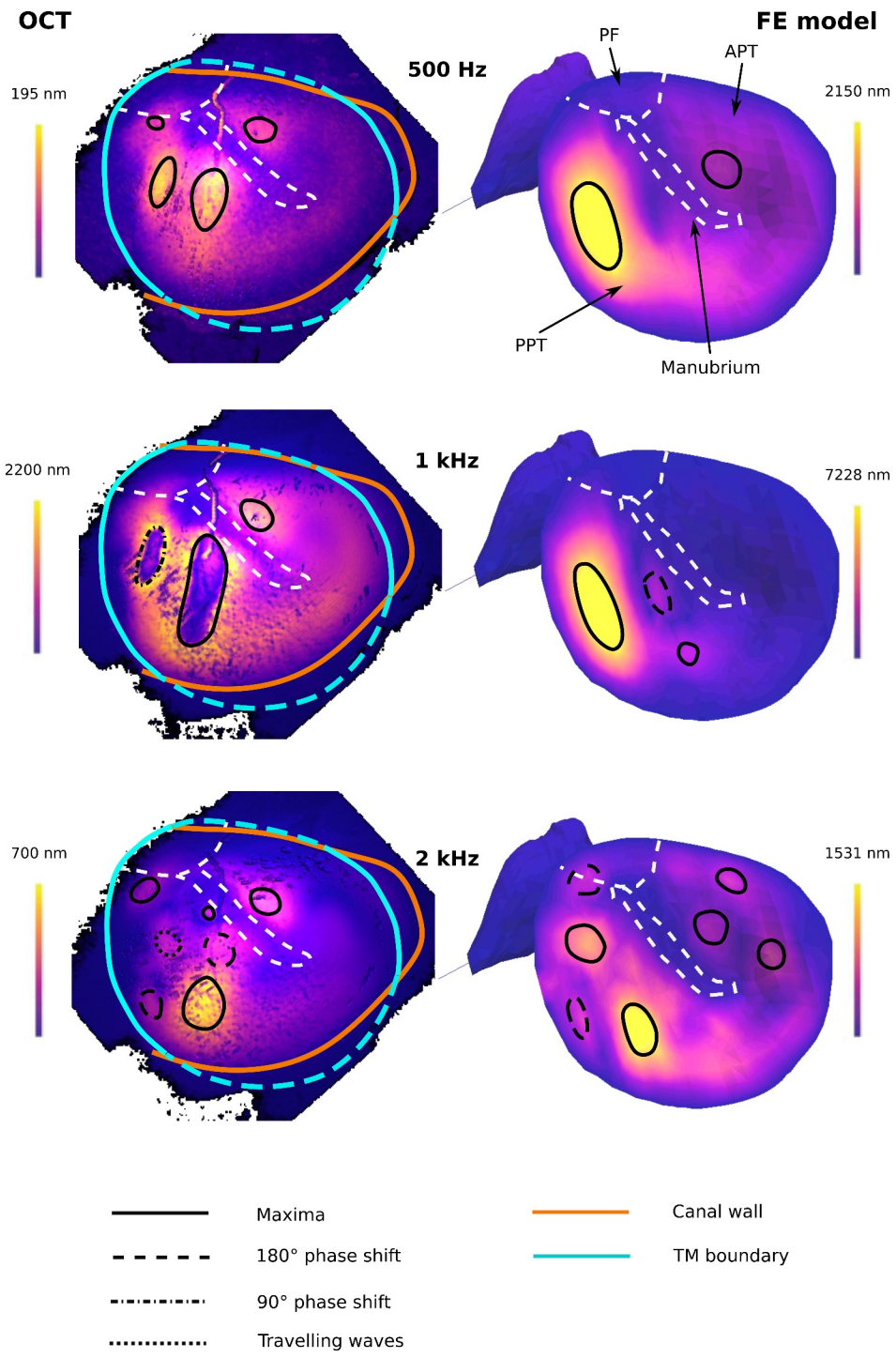

Fig. 6 Vibration displacement maps from OCT measurements and FE simulations at 500 Hz, 1 kHz and 2 kHz for ear 2017-1. PPT = posterior pars tensa, APT = anterior pars tensa, PF = pars flaccida

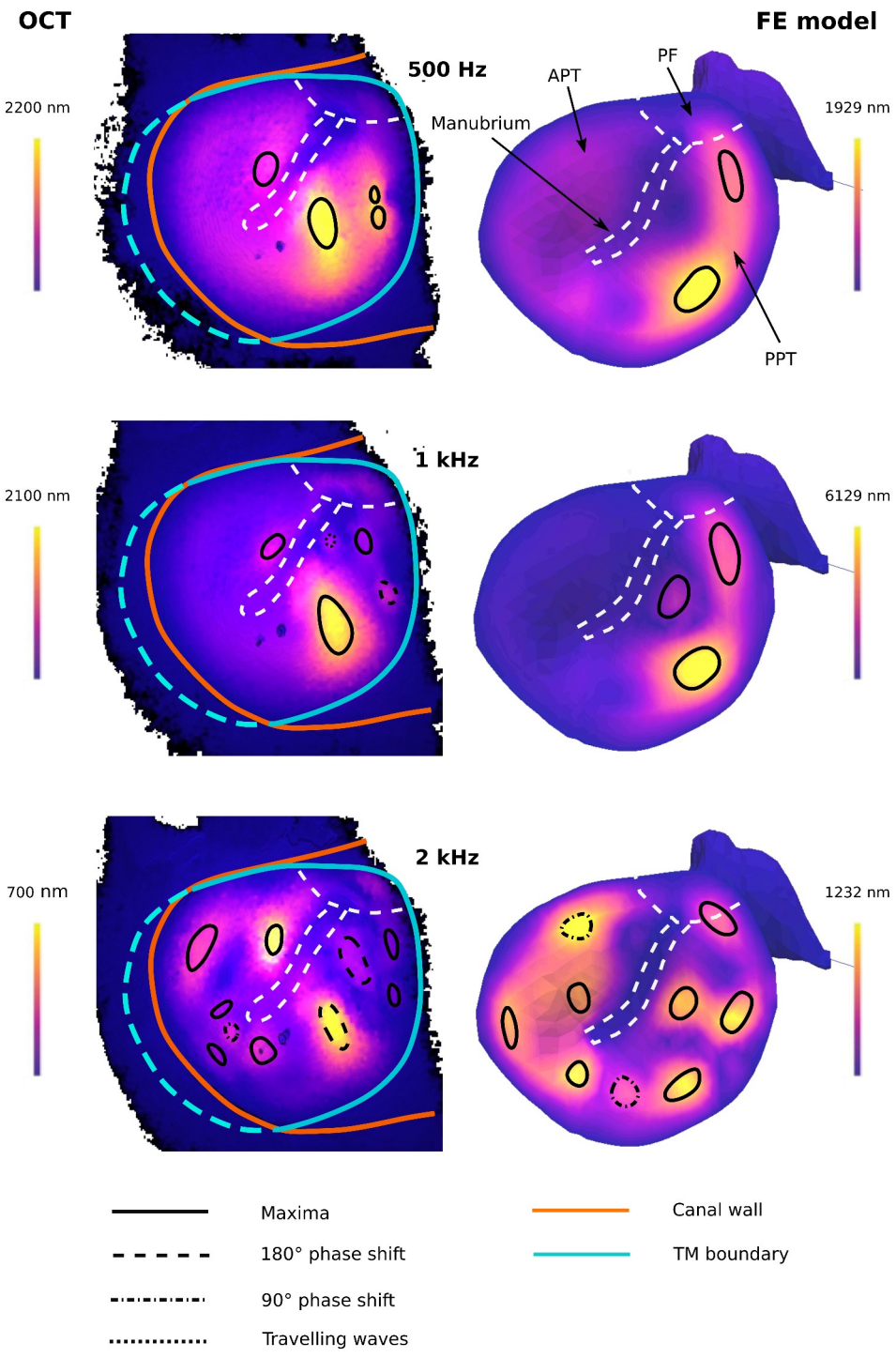

Fig. 7 Vibration displacement maps from OCT measurements and FE simulations at 500 Hz, 1 kHz and 2 kHz for ear 2017-2. PPT = posterior pars tensa, APT = anterior pars tensa, PF = pars flaccida

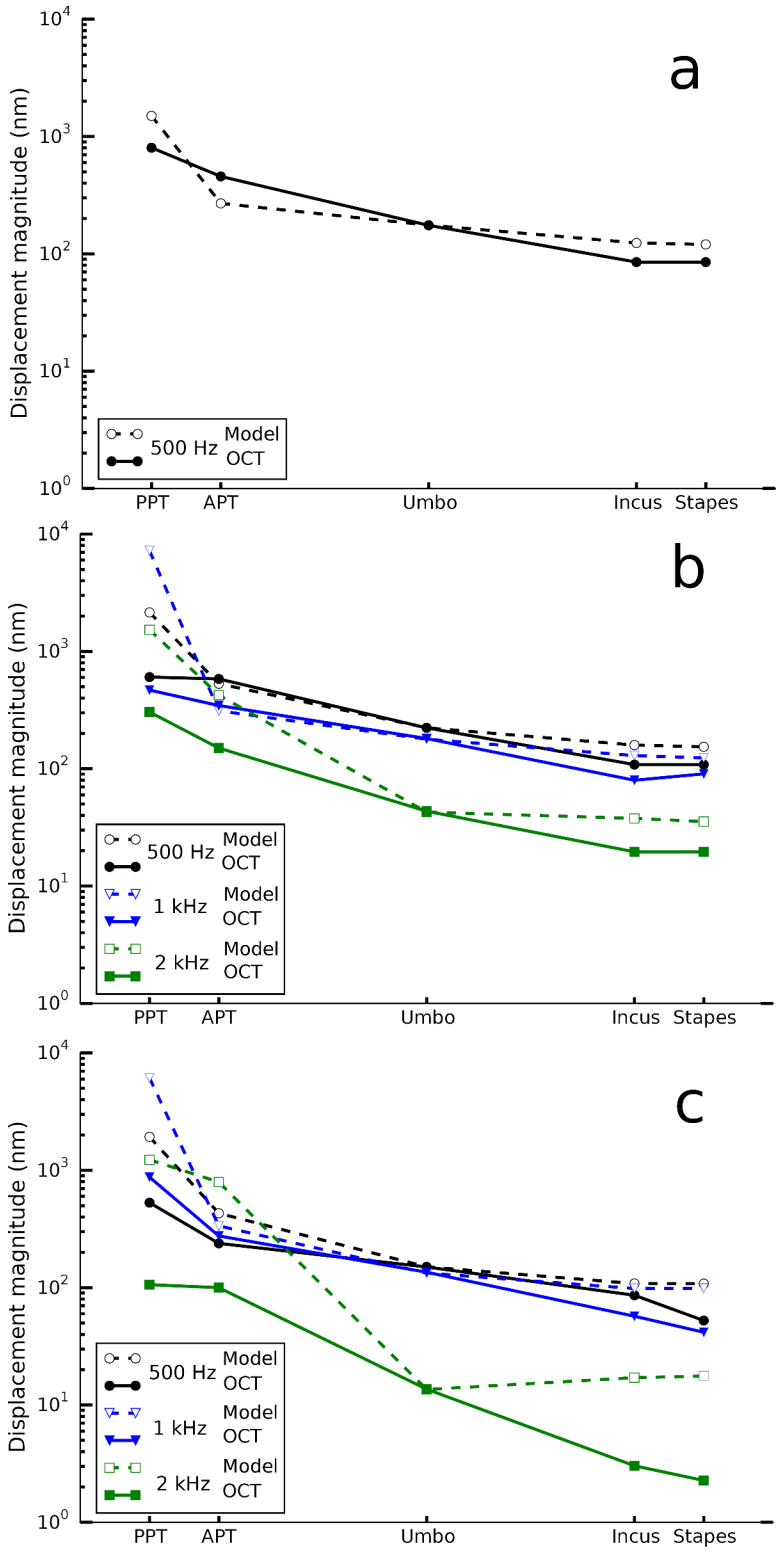

Fig. 8 Displacements for five locations of the middle ear. (a) ear 2016-1, (b) ear 2017-1, (c) ear 2017-2. Dashed lines are for simulated results, solid lines are for experimental OCT data scaled as described in the text

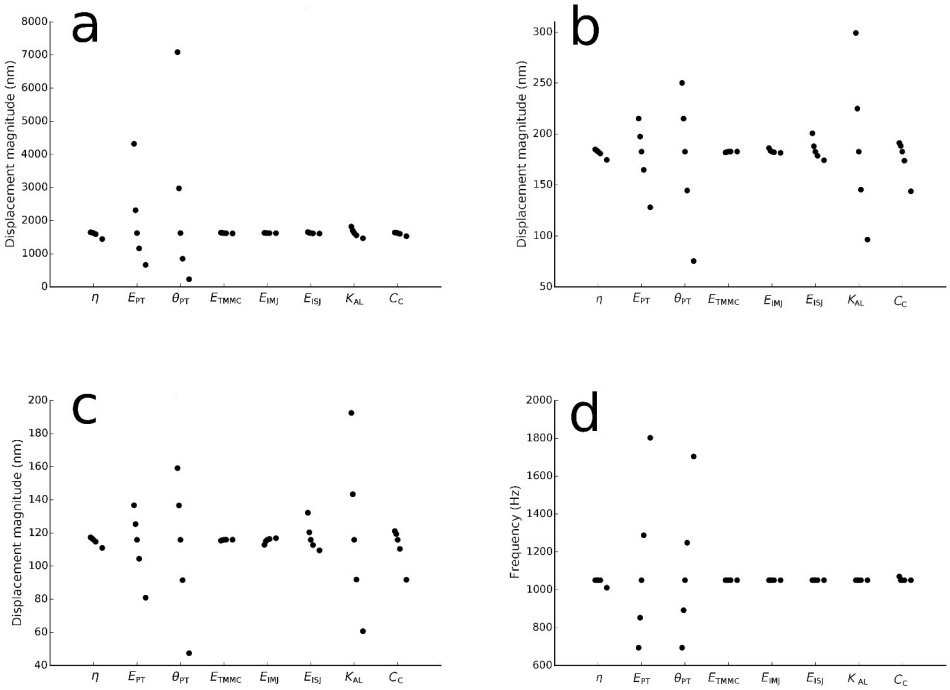

Fig. 9 Sensitivity analysis. (a) maximum displacement magnitude on PT, (b) displacement magnitude at umbo, (c) displacement magnitude on stapes, (d) resonance frequency of PT. The horizontal line indicates different parameter values. θ_{PT} = thickness of pars tensa, E_{PT} = Young's modulus of pars tensa, C_C= cochlear damping, E_{IMJ} = Young's modulus of incudomallear joint, E_{ISJ} = Young's modulus of incudostapedial joint, E_{TMMC} = Young's modulus of TM-malleus connection, K_{AL} = stiffness of stapedial annular ligament, η = loss ratio

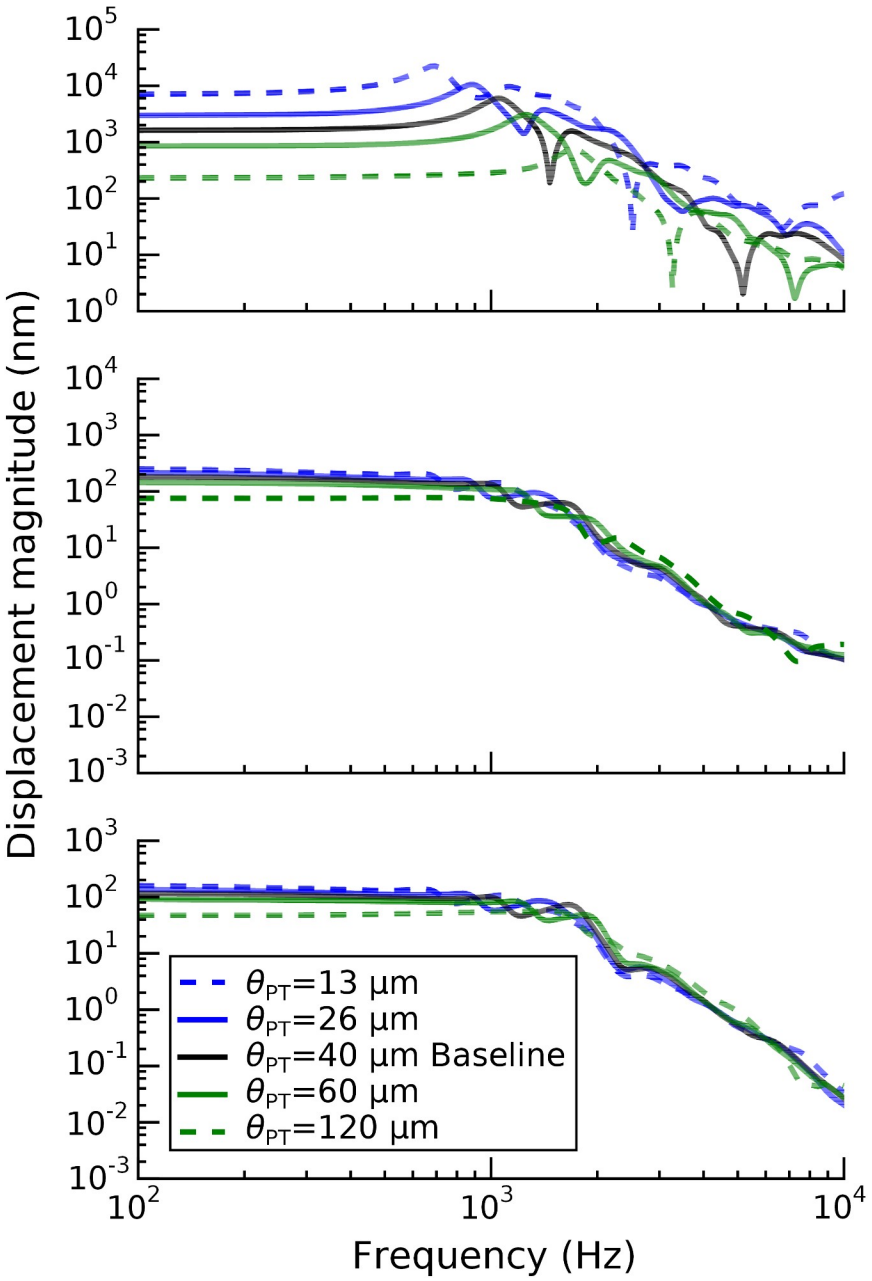

Fig. 10 Effects of θ_{PT} (thickness of pars tensa) on frequency response of FE model for ear 2017-2. Top set of curves is for PT, middle set is for umbo, bottom set is for stapes

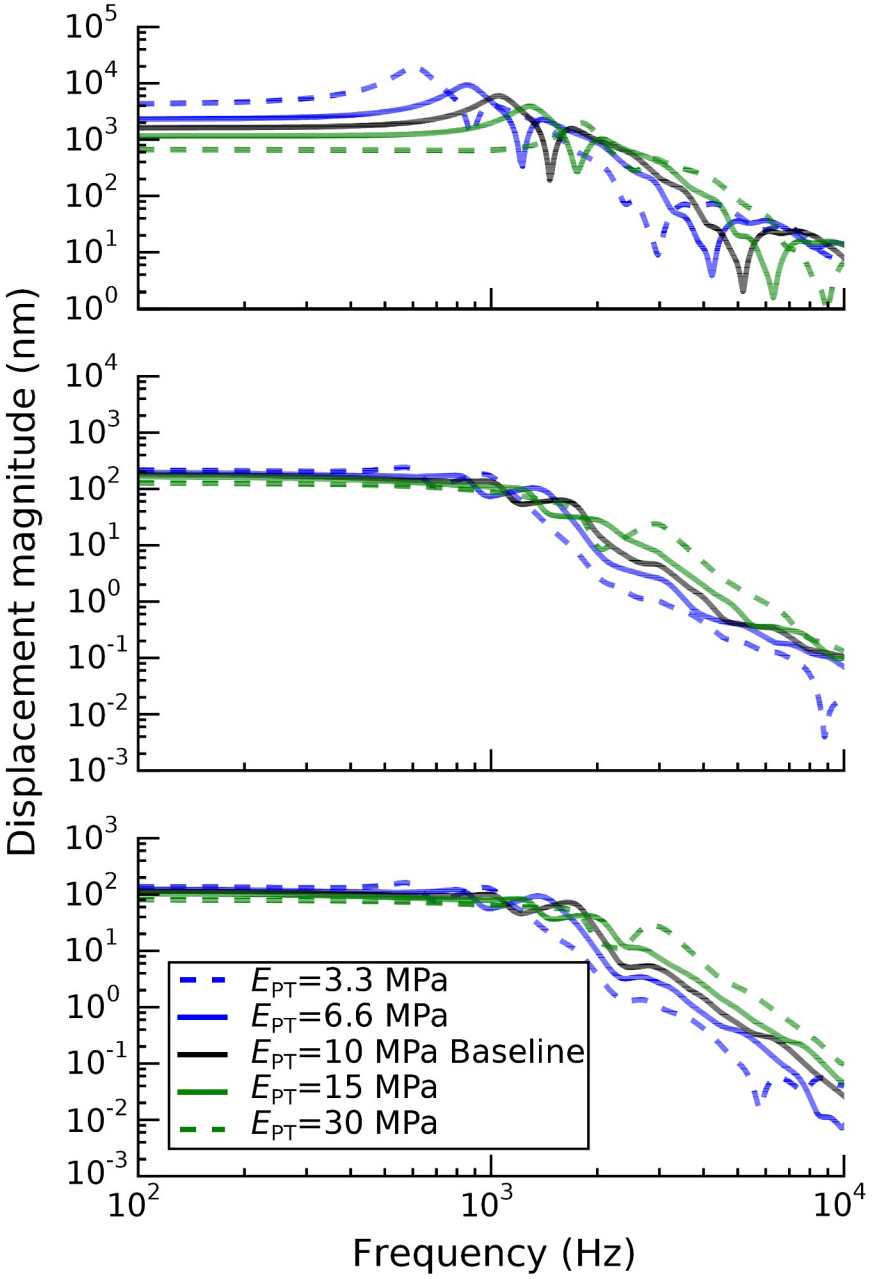

Fig. 11 Effects of E_{PT} (Young's modulus of pars tensa) on frequency response of FE model for ear 2017-2. Top set of curves is for PT, middle set is for umbo, bottom set is for stapes

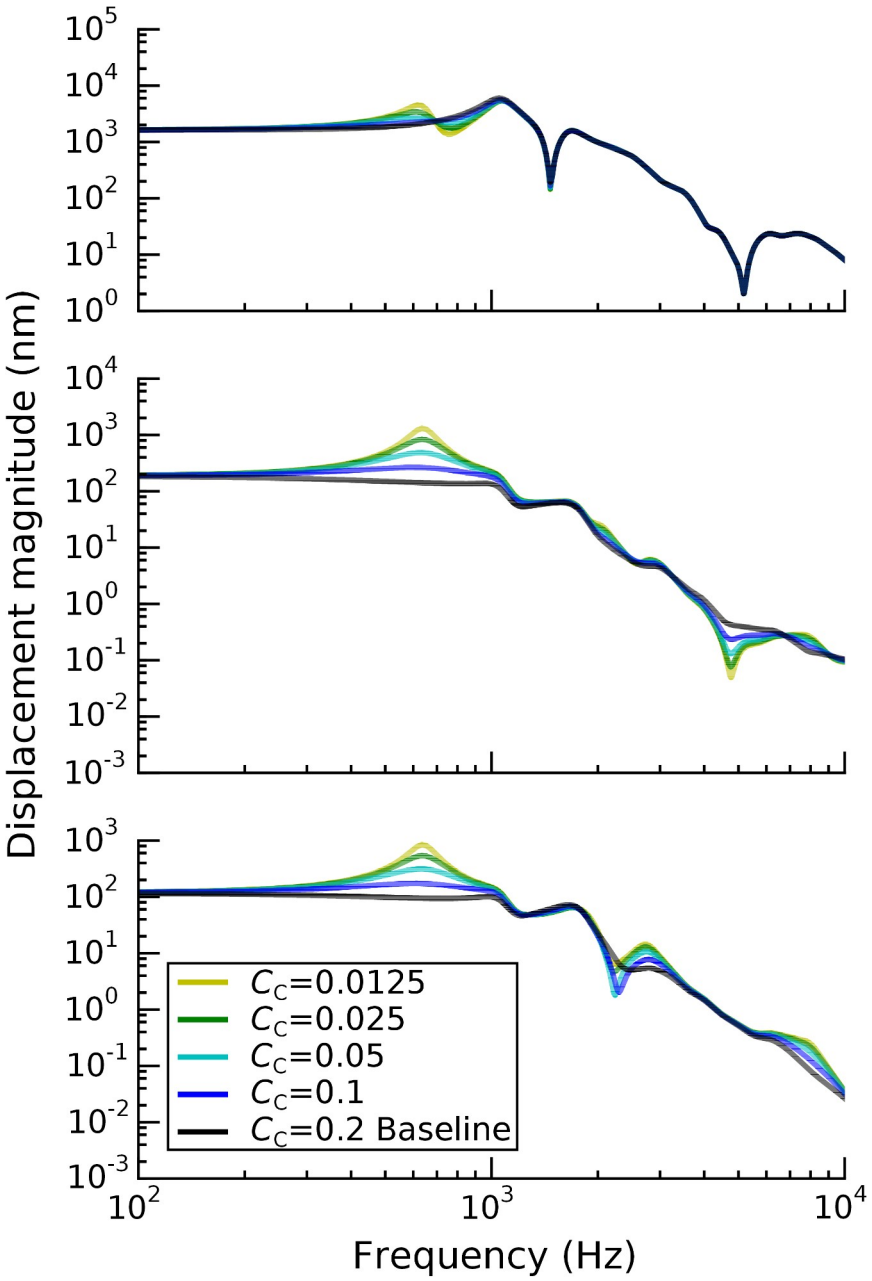

Fig. 12 Effects of C_C (cochlear damping) on frequency response of FE model for ear 2017-2. Top set of curves is for PT, middle set is for umbo, bottom set is for stapes

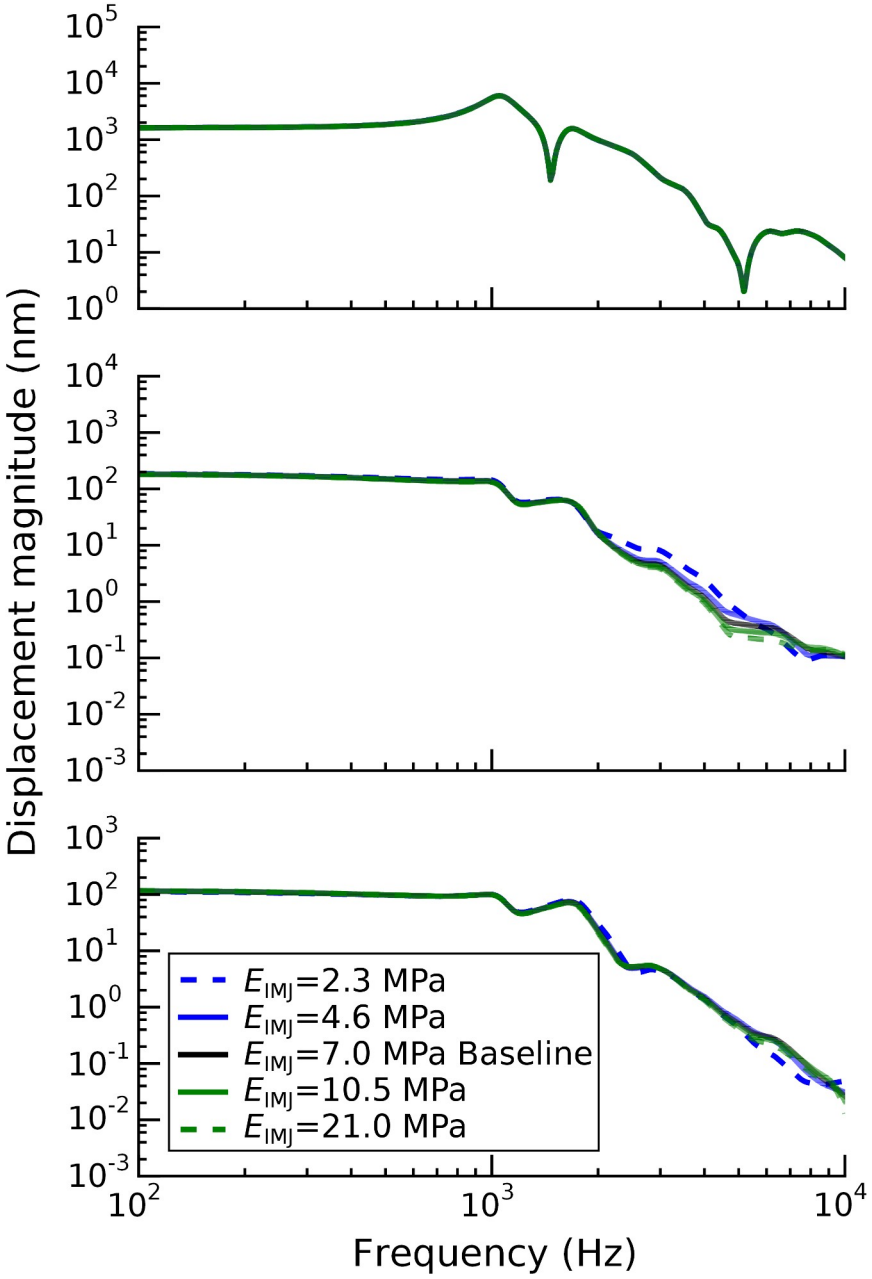

Fig. 13 Effects of E_{IMJ} (Young's modulus of incudomallear joint) on frequency response of FE model for ear 2017-2. Top set of curves is for PT, middle set is for umbo, bottom set is for stapes

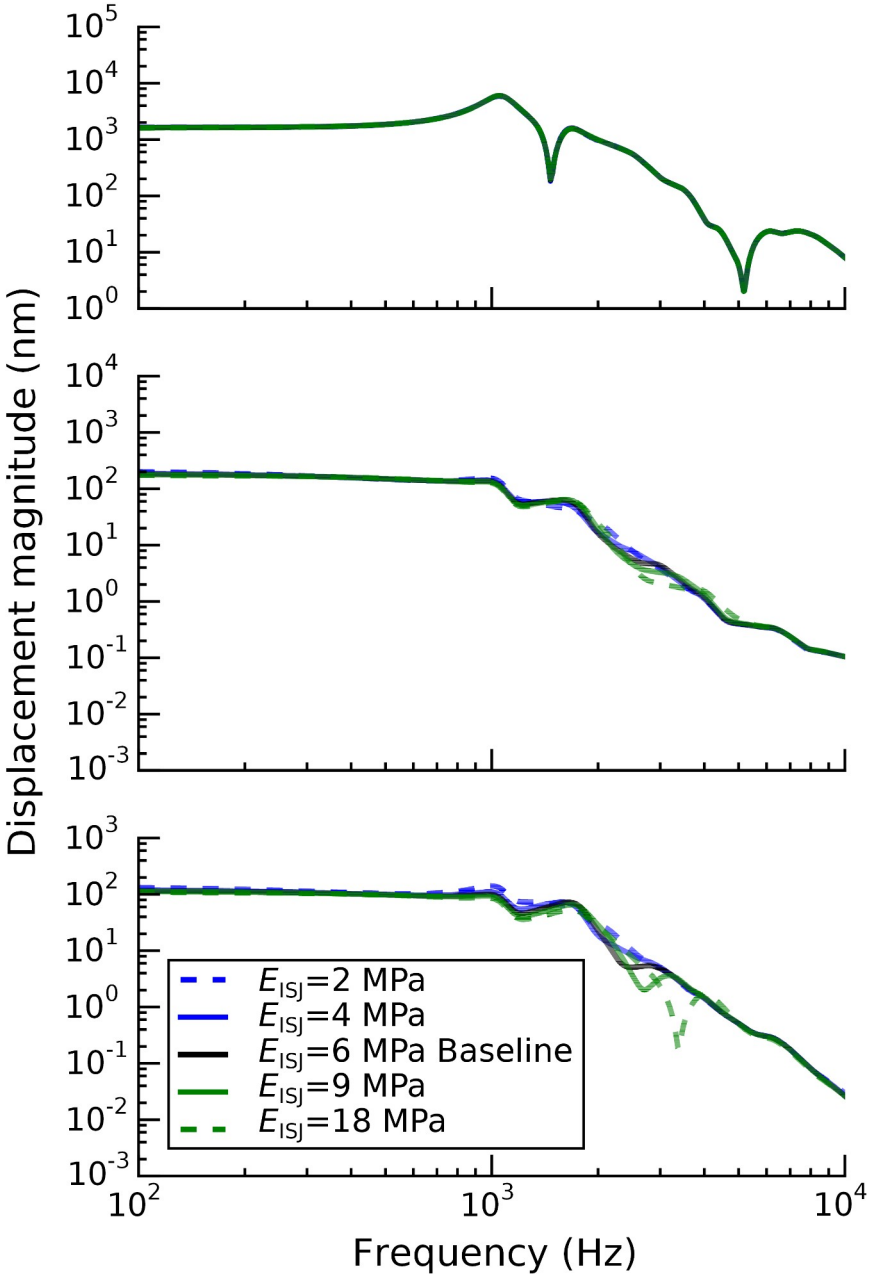

Fig. 14 Effects of E_{ISJ} (Young's modulus of incudostapedial joint) on frequency response of FE model for ear 2017-2. Top set of curves is for PT, middle set is for umbo, bottom set is for stapes

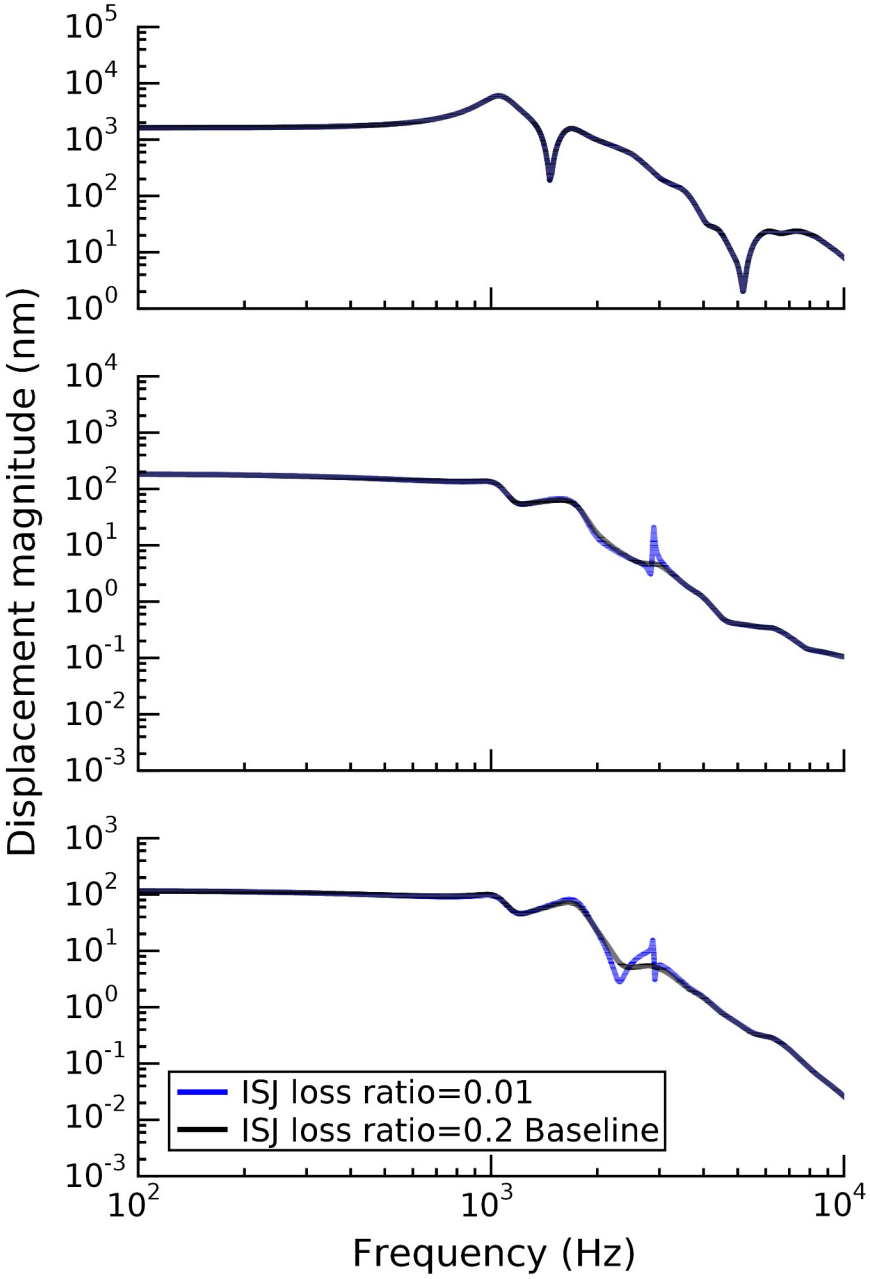

Fig. 15 Effects of ISJ loss ratio on frequency response of FE model for ear 2017-2. Top set of curves is for PT, middle set is for umbo, bottom set is for stapes

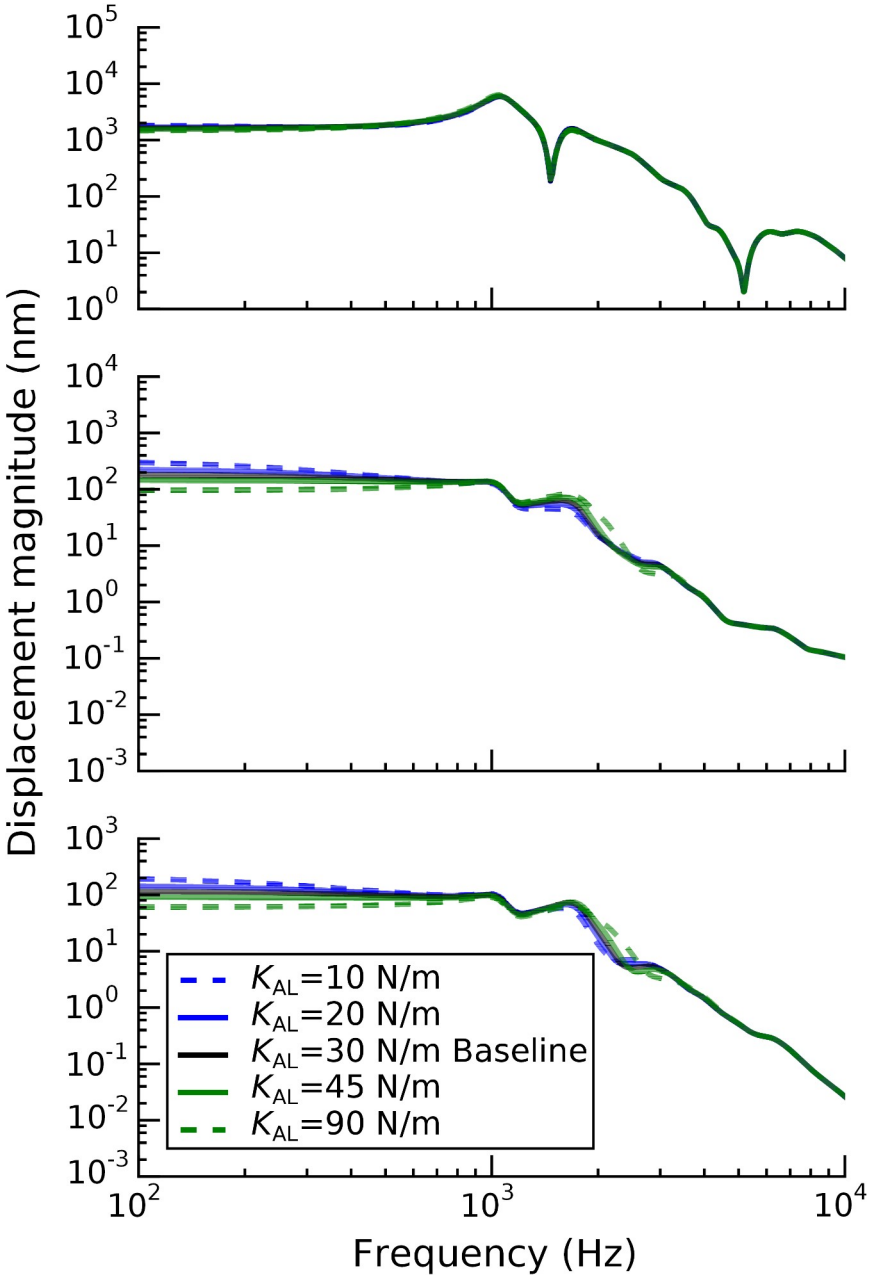

Fig. 16 Effects of K_{AL} (stiffness of stapedial annular ligament) on frequency response of FE model for ear 2017-2. Top set of curves is for PT, middle set is for umbo, bottom set is for stapes

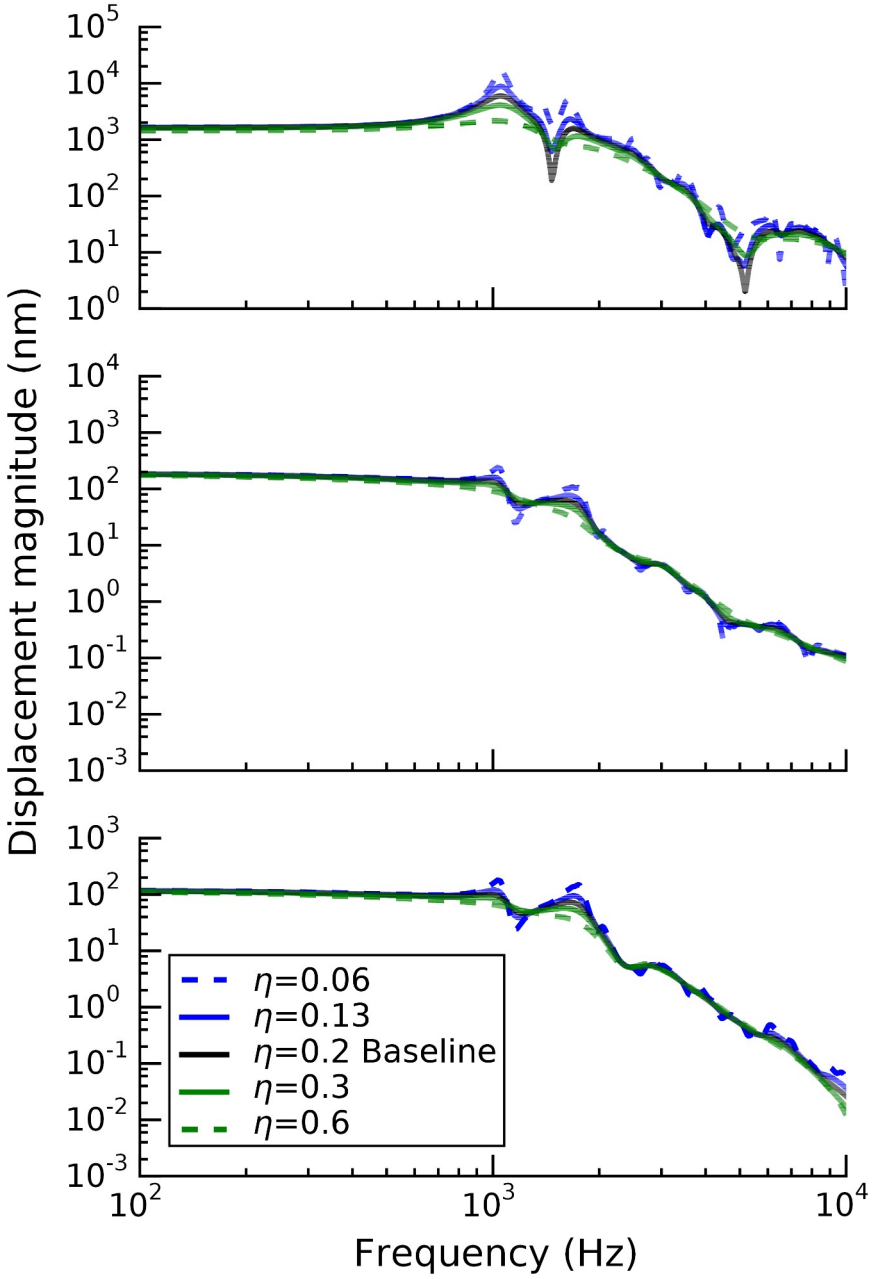

Fig. 17 Effects of η (loss ratio) on frequency response of FE model for ear 2017-2. Top set of curves is for PT, middle set is for umbo, bottom set is for stapes